

Article

The Guided Ultrasonic Wave Oscillation Phase Relation Between the Surfaces of Plate-like Structures of Different Material Settings

Liv Rittmeier ^{1*}, Natalie Rauter ², Andrey Mikhaylenko ², Rolf Lammering ² and Michael Sinapius ¹

¹ Institute of Mechanics and Adaptronics, Technische Universität Braunschweig, Langer Kamp 6, 38106 Braunschweig, Germany

² Institute of Mechanics, Helmut-Schmidt-University/University of the Federal Armed Forces Hamburg, Holstenhofweg 85, 22043 Hamburg, Germany

* Correspondence: l.rittmeier@tu-braunschweig.de; Tel.: +49-531-391-2682

Abstract: Lamb waves occur in thin-walled structures in two wave modes—the symmetric and the antisymmetric mode. Their oscillation on the structures' surfaces is either in phase (symmetric) or shifted by a phase angle of π (antisymmetric). In this work, a method is developed by which to compare the surfaces' oscillation phase relation to answer the question of whether fiber metal laminates show the same surface oscillation behavior as described for metals. The evaluation of time signals regarding the instantaneous phase angle is performed by using the continuous wavelet transformation and the short-time Fourier transformation. Numerical simulations utilizing the finite element method provide time signals from the top and bottom surface of different thin-walled structures of different material settings and configurations. The numerically obtained time signals are evaluated by the developed methods with respect to the oscillation phase. Subsequently, the oscillation phase is evaluated experimentally for the wave propagation in a fiber metal laminate. It is shown that the method based on the continuous wavelet transformation is suitable for the evaluation of oscillation phase relations in time signals. Additionally, it is proven that fiber metal laminates show only two phase relations, which indicates the occurrence of Lamb waves.

Keywords: guided ultrasonic waves; continuous wavelet transformation; instantaneous phase angle; oscillation phase; numerical simulation; finite element method



Citation: Rittmeier, L.; Rauter, N.; Mikhaylenko, A.; Lammering, R.; Sinapius, M. The Guided Ultrasonic Wave Oscillation Phase Relation Between the Surfaces of Plate-like Structures of Different Material Settings. *Acoustics* **2023**, *5*, 136–164. <https://doi.org/10.3390/acoustics5010009>

Academic Editor: Michel Darmon

Received: 18 December 2022

Revised: 18 January 2023

Accepted: 26 January 2023

Published: 31 January 2023



Copyright: © 2023 by the authors. Licensee MDPI, Basel, Switzerland. This article is an open access article distributed under the terms and conditions of the Creative Commons Attribution (CC BY) license (<https://creativecommons.org/licenses/by/4.0/>).

1. Introduction

Structural health monitoring (SHM) by using guided ultrasonic waves (GUW) has been the subject of research for several years. Due to their low attenuation behavior, GUW propagate over large distances without severe signal loss and can be used to monitor large areas. Their property to interact with structural inhomogeneities such as cracks and delaminations makes them suitable for structural monitoring.

GUW appear in two different wave modes, the symmetric and the antisymmetric wave modes [1]. These two modes differ in the direction of the displacement with respect to the midplane of the plate. Regarding the out-of-plane component of the symmetric mode, the phase relation between the structure's surfaces corresponds to the point symmetry relation of an odd function such as the sine-function [2]. This can be interpreted as a phase shift between the upper and lower surface of π . In contrast, the out-of-plane component of the antisymmetric mode behaves like a symmetric function such as the cosine function. This means that the upper and lower surface oscillate in phase [1]. In anisotropic laminates i.e., fiber-reinforced composites, the calculated displacement fields show the same phase relation as described in detail in [2]. In contrast to these displacement field symmetry conditions, the propagation of GUW in honeycomb and foam sandwich structures behaves differently. They show the behavior of Rayleigh surface waves for undamaged structures

without penetrating the core when higher excitation frequencies are used. In [3], sandwich structures with different core height as well as a honeycomb structure with debonded areas are investigated. Propagation of GUV in these structures shows mode conversion from GUV to Rayleigh surface waves for higher frequencies [3], which results in the change of wavelengths. It was also shown that for higher frequencies, the energy transferred from one specimen surface through the core to the other specimen surface for the GUV is damped throughout the thickness of the sandwich structure i.e., fed to the Rayleigh surface wave [3].

The GUV signals that are captured via different measurement methods need further signal analysis and processing to allow an interpretation of the wave propagation properties. In the literature, numerous different signal processing techniques can be found as some are presented in an exemplary manner in [4], offering the time-frequency representation (TFR) as a powerful tool for the analysis of signal features.

The Fourier transformation (FT) is used to gain knowledge about the frequency spectrum of a time signal [5]. The FT assumes that all oscillations can be represented by a summation of sinusoidal oscillations of different frequency, magnitude, and instantaneous oscillation phase [5]. The short-time Fourier transformation (STFT) applies the FT to a small, windowed time signal element whereas the rest of the signal is disregarded. The energy spectrum of the complete signal is created by moving the segment window forward until the complete signal is analyzed. This procedure has a drawback in terms of precision because the window size stays constant [6]. The continuous wavelet transformation (CWT) is a well-known transformation procedure for processing GUVs that uses two parameters, scale, and time to adjust a time-limited wavelet function to the course of a time signal [6]. In comparison to the STFT, a variable window size is used, which is adjusted to the instantaneous size of the signal segment under investigation. This leads to a higher precision in both the time- and frequency-domain simultaneously [6]. It offers full signal information and allows a localization in time and frequency domain [6]. Therefore, it is used for the evaluation of energy distribution in signals over time. This serves the identification of damage when the absolute values of the complex-valued transformation are taken into account [6]. The CWT leads to complex-valued CWT coefficients. The absolute value of these represent the energy distribution. In addition to this, the complex values of the CWT also contain instantaneous phase angle information per frequency per point in time. Little research has been done regarding and using the phase angle gained by CWT applications so far. One aspect that has been dealt with is the concept of the instantaneous phase (IP) gained by the Hilbert transformation (HT). In this method, the phase angle is obtained from an analytic complex signal, which is built from the real-valued time signal $x(t)$ and its real-valued Hilbert transform $H[x(t)]$. Deducing an envelope function $a(t)$ and a phase function $\theta(t)$ leads to the complex representation $z(t) = a(t)e^{j\theta(t)}$ from which the instantaneous Hilbert phase can be derived for the real-valued time domain signal $x(t)$ [7]. Although it is hardly established in engineering applications, the concept of IP has found its way into neuroscience, where it is used intensively to evaluate signals like captured fast transitory signals of brain activity. The need for the synchrony estimation between biological signals has initiated the search for methods that allow the comparison of signal phases. One example is the estimation of phase-locking between two distant brain recordings (i.e., they are recorded by EEG, meaning the detection of a constant phase difference between two signals for a limited time window [8]). Because some noise and fluctuation is to be expected in the brain signals, statistical methods need to be added to allow statements about signal synchrony. This means that the estimation of the IP of the signals must be followed by statistical procedures that allow quantification of the phase relation. The estimation of the IP by using HT and convolution with a complex wavelet are presented in [8] as two principle approaches for the quantification of phase synchrony between neuronal signals. The authors compared the two methods on different signal sets regarding their suitability for the study of neuroelectrical signals. In [9], an algorithmic method is developed for the extraction of instantaneous frequency and IP information in

captured oscillations in the olfactory system of rats. The processed signals contained one or more oscillatory frequencies. The method is based on the CWT and was tested on a synthetic signal to extract the IP. A comparison with the state-of-the-art HT was performed. Although the neuroelectrical signals occur in frequencies between approx. 10–80 Hz [9] (in the olfactory system in rats) and approx. 1–100 Hz [8] (brain activity in humans), the engineering applications using G UW reach to much higher frequencies.

The concept of the IP has also been used for damage detection in the engineering field. In [7], the change in the phase and the time-of-flight of propagating longitudinal wave modes is investigated in damaged and undamaged pipes. This approach is a qualitative method for damage identification and independent from the quality of the transducer bonding, i.e., independent from the signal strength. The sensitivity of G UW modes to delaminations in laminated aluminum plates is investigated in [10]. In the work, the time signal is first processed through a method of mode decomposition to allow the application of the HT as suggested. After having decomposed the time signal into several parts, the HT has been applied to each mode and the IP per mode has been estimated. Subsequently, the IPs per mode are summed to build a total IP which has the property of increasing monotonically as a function of time. The time course of the IP can give indications for existing delaminations showing specific variations.

Another application case is the compensation of temperature effects as a change of the temperature and hence, the material properties influences the G UW propagation. As described in [11], the comparison of a baseline measurement and a measurement under temperature influence may lead to a mismatch in the wave modes due to signal stretching in the time domain. Hence, the authors have developed a method for temperature compensation, which is based also on the time signals' IP derived by the HT. The mismatch, i.e., stretch between the baseline signal and a signal under thermal influence are identified as a change of the IP of the signals. Knowing the phase relation, the shift of the signals can then be compensated mathematically. The analytical signals are converted back to the time domain afterwards, which offers a temperature compensation [11].

In [12], a method for wave mode identification in the context of acoustic emission monitoring is developed. The authors use the phase in combination with the instantaneous frequency information to determine the different wave modes in complex structures. Due to the complexity of the carbon fiber-reinforced polymer (CFRP) structure used, the reflected waves overlap and therefore cannot be distinguished in the time domain. The sensitivity of the method to small changes in phase, the simple implementation of the HT and the independence of the signals' amplitudes allow the occurring wave modes to be reliably identified. In [13], adhesive defects on a glass fiber-reinforced polymer (GFRP) sample are located, sized and characterized using different signal processing techniques for G UW applications. The authors also apply the HT, but use the derived instantaneous amplitude instead of the phase information. It is noted that in G UW processing there is the necessity to decompose harmonics properly to apply the HT. In [14], the authors develop a G UW-based damage imaging condition method for the detection of barely visible impact damages. Therefore, the interaction of the G UW with the damaged area is observed. The interacting waves show a change in the wave number at the damaged location which are identified by using the Riesz transform (RT). The RT is a 2D-HT from which instantaneous amplitudes and phases can be derived for further processing and interpretation of instantaneous 2D wave field images. The IPs used in the work are derived in reference to the direction normal to the propagating wavefront in a 2D representation. A method for defect detection in anisotropic plates by using G UW is proposed in [15]. In the presented work, the HT is used to derive the phase relation between an emitter and receiver via emitter–receiver signal combinations by using a linear sensor array consisting of several piezoelectric elements [15]. In [16], the IP characteristics of shear horizontal waves are used for the detection of various defects in an aluminum specimen. The shift in the IP of the shear horizontal waves shows different patterns for different defects. In geophysics, Yuan et al. [4] define the concept of

the exponentiated phase (EP) by using a normalization of the HT by its corresponding time-dependent envelope function. This concept allows a steady application to seismic signals.

Examples that the phase information derived by the CWT, which cover the field of medical research and civil engineering, are presented in the following. In [17], the CWT is used for electroencephalography signals to extract magnitude and phase information at the same time. With both the magnitude and phase information, neural networks are trained. In the field of civil engineering, the complex continuous wavelet transformation (CCWT) is utilized to decompose a single time domain signal and to separate it into different time domain signals per frequency [18]. The phase information per time domain signal is used for phase observation. CCWT is used to identify defects in piles by observing phase changes in the 3D phase spectrogram. In this context, the 3D phase spectrogram is the IP angle derived from the CWT coefficients [18]. With the information about the location of the phase inversion in the time domain, damage is detected. The time difference allows one to derive defect location. Furthermore, the wavelet transformation based on a modified complex Morlet wavelet with variable center frequency is applied to seismic response data to gain the phase information [19]. Again, the objective is to detect damage. This is done considering the phase of each measurement, i.e., the phase of each sensing node for different test cases. The phase angles of the individual analyzed frequencies of the recorded signals show changes in case of damage. The location of damage is derived by the sensing node position in which a phase angle change occurs [19]. The major objective is the reconstruction of the time signal of an earthquake response from the complex wavelet coefficients. Therefore, the calculation of the unwrapped phase is performed by selecting frequency bands of interest. For this, the complex values along the bandwidth are summed, which leads to a coefficient sum per time step. These obtained complex values are then used to calculate the IP at each particular time step [19]. It is shown that the concept of an IP gained from analytical signals mostly created by the HT are used in wavefield analysis especially in damage detection applications and neuroscience. However, it needs to be verified whether the approaches used in neuroscience can be transferred to G UW at higher frequencies. In [9], the IP extracted by HT and the wavelet transformation are compared. As a drawback of IP that uses the angle of the HT, it is found that the time signals require an appropriate filtering before transformation to obtain accurate estimates of the phase. Good phase results can be obtained by filtering, but at the cost of losing time and frequency information [9].

However, phase evaluation methods based on the Hilbert IP do not consider the phase relation of different frequency components, but evaluate a time signal as such. For a multifrequency signal, it needs to be taken into account that different frequency components may have different phase relations. Furthermore, the description of the oscillation phase relation in G UW has so far been valid for isotropic and anisotropic materials. It is to be examined whether this assumption can be transferred from G UW to fiber metal laminates (FML). It was shown experimentally that the oscillation in FML not only propagate through the covering layer but also penetrate the thickness of the laminate, so there is no experimental verification about possible phase delays and shifts of the surface oscillations [20].

The major objective of this work is therefore, the investigation whether there is a phase shift between the upper and lower surface oscillation of plate-like structure fabricated from FML. This is of particular interest because FML consist of the combination of materials with very different wave propagation velocities. Wave propagation behavior remains to be characterized depending on the difference in acoustic impedances and their change within the laminates. Because the HT is insufficient when a signal shows many wave modes overlapping, different approaches will be investigated in this work [6]. Regarding signal transformation procedures such as STFT and CWT, it can be seen that IP angle information is stored in the transformation parameters and therefore is evaluated with regard to the suitability for phase angle evaluation.

Following the different wave propagation patterns of GUV in pure fiber-reinforced polymer (FRP) and sandwich structures as well as the suitability of the CWT to extract phase information over time of a signal, the CWT is evaluated in this work to analyze the wave propagation characteristics in structures with different grades of complexity and impedance changes over the thickness. Hence, the work focuses on both experimental and numerical investigation based on laminates made from different solid materials. It is analyzed whether the propagating wave modes show the same oscillation phase behavior at the surface as described in the analytical framework of GUV. In this context, phase angles different from π or 0 indicate a wave propagation behavior that differs significantly from the analytical framework of GUV in thin-walled structures.

This work addresses two objectives. The first is the development of a procedure to compare the oscillation phases of time signals across a certain bandwidth while allowing a reference to time segments of the analyzed signals. The second objective is to investigate whether FML show the same surface oscillation behavior under GUV excitation as composites or metals. In the first step, two methods of oscillation phase angle evaluation are derived and presented. As mentioned above, a method based on the CWT comparing the oscillation time signals of the two surfaces of plate-like structures and the STFT. In this approach, the upper and lower structure surface spectra thus obtained are related by subtracting them and interpreting the phase difference in terms of the analytic phase relation for GUV.

In the second step, the developed evaluation methods are applied to numerically obtained time signals showing the noise-free GUV propagation in four different specimen material setups for the upper and lower structure surface. The specimens prepared from different material settings are considered to identify various possible factors influencing the phase angle relation. The plate specimens differ regarding the amount of material interfaces, stiffness characteristics, amount of materials and fiber content to enable a step-by-step examination of the different settings.

In the third step, the wave propagation is measured on FML test specimens to gain experimental time signal data and to validate the approach. The derived methods are then applied to the authentic measurements. They are evaluated with regard to their oscillation signals on the upper and lower surface. The work closes with an evaluation of the work and outlook of future work.

2. Materials and Methods

This section describes the different configurations of the test specimens. Signal-transformation methods are presented, and their advantages and drawbacks in terms of phase evaluation are discussed.

2.1. Specimen Design

Four different material configurations are chosen for the experiments: an aluminum plate, a steel-film adhesive laminate made from two steel layers and a film adhesive in between, a simplified aluminum-GFRP laminate with unidirectional GFRP similar in its setup to GLARE 2A [21], and a GLARE 3-3/2-0.4 plate. The specimens are chosen this way to represent different structural conditions. The aluminum plate represents an isotropic, homogeneous metal. The steel-film adhesive laminate is an isotropic structure that consists of three layers with different stiffnesses resulting in two material interfaces. The aluminum-GFRP laminate consists of a top and bottom layer of aluminum with four layers of unidirectional GFRP in between. In addition to the anisotropic material behavior due to the GFRP layers, two material interfaces are generated. The GLARE 3-3/2-0.4 plate offers the highest degree of complexity, namely with the challenge of more interfaces between metal and FRP as well as different fiber directions.

With these four different specimens, the influence of the fiber content, number of interfaces, and the combination of different material symmetries on the oscillation phase between the upper and lower structural surfaces can be investigated systematically. Both

the numerically obtained and experimental data are used. In addition to the variation of the materials, the extent to which the evaluation of the fundamental modes differs from the evaluation of the higher order modes is investigated. For this purpose, excitation frequencies are chosen that already provide higher-order modes for two laminates but not for the other two structures. Different degrees of complexity in the investigations can be realized. An overview of the specimens' variants is given in Table 1. The chosen excitation frequencies reach from 200 kHz to 300 kHz and lie within the standard frequency range for SHM using GUV but are still low enough for a sufficient amplification by the used voltage amplifier in the experiment.

Table 1. Overview of the selected specimens and their structural characteristics.

Specimen Type	Fiber Reinforcement	Interfaces	Stiffness Characteristics	Number of Constituents
Aluminum	no	0	isotropic	1
Steel-Film Adhesive	no	2	isotropic	2
Aluminum-GFRP	yes	2	transversely isotropic	2
GLARE 3-3/2-0.4	yes	4	orthotropic 0°/90°	2

2.2. Fundamentals of the Signal Evaluation

Spectra obtained with the STFT or the CWT show as standard the energy distribution, i.e., the magnitude or the absolute values of the complex values gained from a transformed time signal. The approach presented here is different because the IP information in relation to its occurrence in the time domain is derived from the transformation parameters. The suitability for the comparison of the signals' phase angles is evaluated in additional steps. A TFR using the CWT preserves time and frequency information while additionally offering a variable window size adjusted to screened frequency of interest [9].

The first signal transformation used is the STFT, which performs a segment-wise FFT analysis of the evaluated time signals. The Fourier integral provided in Equation (1) gives the complex-valued Fourier transform $X(j\omega)$

$$X(j\omega) = \int_{-\infty}^{\infty} x(t)e^{-j\omega t}, \quad (1)$$

which can be decomposed into a real and an imaginary part

$$X(j\omega) = \Re X(j\omega) + j\Im X(j\omega) \quad (2)$$

holding information about the phase angle [22].

Because the STFT is based on the Fourier principle, the transformation leads to these complex values, which contain a magnitude and phase information of the oscillation per extracted frequency component per time segment. The phase can be extracted for each corresponding frequency component in the regarded signal section. It represents how each signal component in the time domain is shifted in the acquired time signal. The captured time signal can be interpreted as a superposition of several oscillations with different frequencies and phase position [5]. For each point in time, the phase per frequency component can be used for a phase comparison between the oscillation on the structural surfaces. The length of the time segment must be specified and needs therefore to be adapted to the characteristics of the time signal. The time segment length influences the uncertainty in the frequency domain and in the time domain, with time uncertainty increasing and the frequency uncertainty decreasing due to K upfm uller's uncertainty principle [23]. The window size cannot be altered leading to the fact that precision in the time domain and the frequency domain cannot be obtained synchronously [6]. It is necessary that the time segments lead to a sufficient resolution in the frequency domain with a good localization in the time domain. Therefore, the optimal time segment length must be found for the corresponding application.

In the following, the CWT is applied by using analytic wavelets. The CWT coefficients are calculated by the integral

$$CWT(a, b) = \frac{1}{\sqrt{a}} \int_{-\infty}^{\infty} x(t) \cdot \Psi^* \left(\frac{t-b}{a} \right) dt, \quad (3)$$

with Ψ^* as the complex conjugate of the orthogonal wavelet function Ψ and $x(t)$ as the time signal to be transformed [6].

In the CWT, a wavelet function with a center frequency of f_0 is dilated by a scale factor a and shifted in time by b . By increasing or decreasing a , the used wavelet function is fitted to a segment of a time signal $x(t)$. Thus, the scale factor a is a frequency representation. The analytic wavelets offer the advantage that they are complex-valued but do not show negative frequencies and make it possible to estimate the instantaneous amplitude and IP of a nonconstant oscillatory signal [18,24]. The wavelet transformation provides IP information associated with a specific location in the time and frequency scale of the evaluated signal, and does not have the drawback of Fourier analysis. Specifically, the FT is not well suited for nonperiodic signals and does not show the relationship between frequency, phase and location in time. The CWT offers the possibility to gain frequency information over time, providing the direct link to the timeframe of occurrence of specific frequencies. It also represents the energy distribution of a signal on the timescale when the transformation results of the CWT are squared [6,9]. The time-frequency-phase diagram deduced from the IPs provided by the CWT is called the 3D phase spectrogram [18]. It covers the angle range from $-\pi$ to π . When additionally divided by the scale a , the representation is normalization, leading to the so-called normalized scalogram representation [9]. When interpreting scalograms, it needs to be kept in mind that an increase of the frequency $\omega_0 = 2\pi f_0$ causes a better frequency resolution, whereas the resolution in the time domain decreases [9].

The extraction of the angle stored in the complex wavelet transform has already been performed and has been proven efficient even on noisy signals [9]. There are as many CWT coefficients as there are time steps per frequency. Therefore, estimating the phase information by using the complex-valued coefficients offers the phase information located in time and frequency. One major advantage of this approach is that it can be used for one complete measurement signal without additional segmentation. Referring to [18] and [6], the IP or phase angle is calculated by using

$$\phi(a, b) = \arctan \frac{CWT_I(a, b)}{CWT_R(a, b)}, \quad (4)$$

with CWT_I and CWT_R being the imaginary and real part of the CWT, respectively. Because there are many wavelets that can be used for the transformation, it is generally advised to use a wavelet with a wave form resembling the evaluated signal as much as possible [6]. An overview of the advantages and drawbacks regarding the suitability for the extraction of phase angles as well as the frequency domain resolution is listed in [25].

2.3. The Concept of the Absolute Phase Difference Spectra

In the following, the concept of absolute phase difference spectra (APDS) is introduced to allow the analysis of the phase angle relation between the upper and lower structural surface. They are based on the phase information contained in the spectrograms derived by STFT and CWT. Hereafter, the theoretical background is explained in detail. In contrast to HT, the presented methods allow the estimation of phase angles along a wide bandwidth to cope with the dispersive nature of the guided waves. An estimation of the phase relation between oscillation components at different frequencies is therefore possible.

2.3.1. Properties and Settings for the Signal Transformation Methods

The implementation of different signal transformation methods requires an adjustment of the transformation settings for the corresponding application. Hence, in STFT, referring to the uncertainty principle described in Section 2, the time segment length is chosen to be

equal to the length of the excitation signal, the length of a five-cycle sinusoidal burst. The excited wave packages' length will be of the order of magnitude of the excitation signals' length assuming a dispersive behavior that is not too strong. This helps to maintain a reference to the location in the time domain and allows an allocation of the existing phase angles. The spectrum output is set to centered and thus provides a two-sided centered spectrum. The chosen time segment lengths offer a frequency resolution of approx. two frequency steps around the center frequency. MATLAB is used for the implementation. The procedure is part of a signal processing toolbox, which is an extension of the software as described in [26]. The created time segments are Hanning-windowed and the overlap length for the STFT is chosen to be 99% of the time segments' length. Overlapping of the time segments avoids information loss in the later SFTF. The precision in the time resolution increases with the overlap.

The CWT algorithm (continuous 1-D wavelet transform) is implemented in MATLAB and uses by default the Morse wavelet. It belongs to the class of analytic wavelets with the advantages described in Section 2.2 [27]. The analytic Morse wavelet with the symmetry parameter equal to 3 represents perfect symmetry of the wavelet in the frequency domain [28]. The sample frequency is deduced from the measurements and used as input parameter for the MATLAB algorithm. The algorithm automatically performs the scale-to-frequency conversion [27]. This offers scalograms with time-frequency representation in which the scales are converted to the frequencies by using the relation $f = \frac{f_0}{a}$ as described in [9,28]. Referring to the MATLAB manual, the minimum and maximum scale in the CWT spectrum, i.e., the maximum and minimum frequency in the frequency interval, are chosen automatically based on the energy distribution of the evaluated signal. The CWT algorithm is set to the highest possible frequency resolution of 48 voices per octave. Because the algorithm automatically chooses the minimum and maximum scale based on the signals energy distribution [28], the amount of voices defines the scale resp. frequency resolution and smoothness of the scalograms.

2.3.2. Theoretical Background of the Absolute Phase Difference Spectra

In contrast to [8], the phase difference of the signals will not be limited to one target frequency, but will cover a frequency range. This is necessary because GUW excitation always covers a frequency bandwidth that leads to the propagation with different group velocities due to the dispersive nature of the GUW. Hence, the spectrograms of the upper and lower surface are subtracted from each other after their computation. This provides the phase angle difference between the two surfaces and allows a reliable comparison of the oscillation relation. The spectra gained in this way are referred to as APDS. During the subtraction, the sign of the phase values can cause phase angle differences, which are not within the interval of 0 to 2π . These angles physically correspond to phase angles between 0 and 2π and can be interpreted as multiples of 2π , i.e., an additional circumnavigation of a unit circle. For the limitation of the APDS to a range from 0 to 2π , the absolute values of the phase difference are chosen. They are deduced as follows:

Compare

$$\frac{\pi}{4} - \left(-\frac{\pi}{4}\right) = \frac{\pi}{4} + \frac{\pi}{4} = \frac{\pi}{2} \quad (5)$$

and

$$-\frac{\pi}{4} - \frac{\pi}{4} = -\frac{\pi}{2} \quad (6)$$

with

$$\left|\frac{\pi}{4} - \left(-\frac{\pi}{4}\right)\right| = \left|\frac{\pi}{2}\right| = \frac{\pi}{2} \quad (7)$$

and

$$\left|-\frac{\pi}{4} - \frac{\pi}{4}\right| = \left|-\frac{\pi}{2}\right| = \frac{\pi}{2}. \quad (8)$$

For later interpretation, the theoretical framework presented in Section 1 allows either no phase difference or a clear phase shift of π between the surfaces. The absolute value of

the phase difference considers the direction of the phase shift between two oscillations but neglects the relative shift in the time domain. This argumentation is plausible with regard to Figure 1. The unit circle on the left side represents the instantaneous position of two oscillation signals in time which provide a certain phase relation toward one another. The phase angle difference is ϕ . The unit circle on the right side also provides two time signals. These are shifted in time compared to the image on the left side, but show the same phase relation, i.e., phase angle difference toward one another.

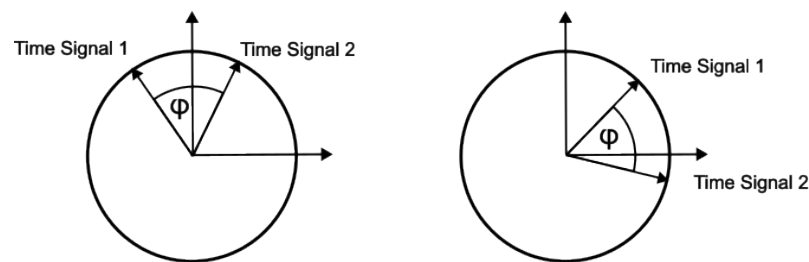


Figure 1. A sketch demonstrating two time signals in the pointer representation: the instantaneous time varies, whereas the relative phase position, and hence, the oscillation phase difference, is the same.

The derived spectra consequently contain the phase angle plotted over the time axis as well as the frequency resolution corresponding to the bandwidth of the excitation signal.

In the following, the introduced concept of the APDS will be used for the evaluation of the phase relation between the upper and lower surface oscillation for the different specimen setups as shown in Table 1. This is done for numerically obtained time signals as well as for measured data. The APDS are calculated by using both signal transformation methods. The APDS of the STFT is referred to as APDS-STFT and the APDS of the CWT is referred to as APDS-CWT.

In order to simplify the representation in reference to [19], the frequency bands of interest are chosen, i.e., the frequency range of the excitation's bandwidth. The graphical representations of the APDS is therefore limited to the approximate signals' bandwidths as a region of interest. Their values at the borders differ slightly between the APDS-STFT and the APDS-CWT due to the different frequency resolution and the different frequency step sizes, respectively. Higher and lower frequencies beyond the signals' bandwidth are mathematical relicts of the transformation procedures and do not have a physical meaning. To simplify the procedure, subsequent statistical processing as mentioned in [8] is omitted.

3. Results of the Application to Numerical Data

Because positioning accuracy and measurement uncertainty can cause additional error sources to experimentally obtained data, the developed methods are first tested and evaluated by using numerically derived time signals. Hence, in this section, the APDS is calculated for time signals that are estimated for the four different material setups introduced in Section 2.1. First, the numerical model, the setup as well as the results of the calculations are presented. Therefore, a two-dimensional model is established, which coincides with the direction of the captured wave propagation in the experiment. The reduction to a two-dimensional model is possible because the wave propagation is only analyzed in a symmetry direction of the material properties, which leads to a decoupling of the material particle motion in the cross-section (x_1 - x_3 -plane) and the out-of-plane component (x_2 -plane).

Secondly, the simulated time signals are assigned to groups regarding their time course characteristics. Following this, the APDS-CWT and APDS-STFT are calculated. The observed patterns are described and interpreted.

3.1. The Numerical Model

In order to be able to compare numerically obtained results with the experimental data in a subsequent step, the same setup is used. This includes the specimen design, the excitation signals and the excitation frequencies as well as the positions of the measurement points. The procedure of the numerical simulation is presented in detail below.

The wave guide is modeled by a cross-section of the experimental specimen consisting of quadratic shaped second-order Lagrange elements as shown in Figure 2. The length of the rectangular model of the laminate cross-section is 0.75 m, whereas the thickness depends on the material layout. Therefore, the thickness of the model depends on the stacking sequence of the modeled laminate. The cross-section is supported by a symmetry boundary condition at the left edge. In addition, the displacement is fixed in the middle of this edge. The excitation is realized by an out-of-plane displacement consisting of a five-cycle Hanning-windowed sine burst with a center frequency of 200 kHz, 250 kHz, and 300 kHz. Finally, the wave propagation is captured at a congruent point on the upper and lower surface of the cross-section, which is identical to the experimental setup.

The numerical simulation is performed for all specimens used in the experimental investigation. Because the numerical model gives an individual representation of each material phase of the different specimen, Table 2 holds the material properties for the isotropic phases aluminum, steel, and the film adhesive as well as the transversely isotropic GFRP.

Table 2. Material properties used for the numerical simulations of the wave propagation.

Material	E_1 [GPa]	E_2 [GPa]	ν_{12} [-]	G_{12} [GPa]	G_{23} [GPa]
Aluminum	72	72	0.33	27.07	27.07
Steel	210	210	0.3	80.77	80.77
Film Adhesive	3.1	3.1	0.36	1.14	1.14
GFRP 0°	54	9.4	0.33	5.55	3.41

Furthermore, for a proper representation of the wave propagation the discretization and the time stepping is essential. The following conditions apply [29,30]:

$$\Delta t_{\max} = \frac{1}{20f_{\max}}, \quad (9)$$

$$\Delta x_{\max} = \frac{\lambda_{\min}}{20}. \quad (10)$$

Here, Δt_{\max} is the maximal time step and Δx_{\max} the maximal element size. Based on these criteria, the time stepping is set in accordance with the excitation frequency. In contrast to this, the determination of the used element size is more complex and depends not only on the wavelength of the generated wave modes, but also on the laminate stacking sequence and the layer thicknesses. To derive the optimal discretization for each specimen, first the equation of motion is solved with respect to the boundary conditions of stress free surfaces for GUW, which gives the expected wavelengths of the different wave modes. Their estimation is based on the methodology described in [2], taking into account the multilayered setup of the investigated FML as well as the assumption of the balance of momentum. The dispersion diagrams are calculated analytically for all four test specimens by using MATLAB.

The results are summarized in Table 3. Furthermore, the values of Δx_{\max} obtained by using Equation (9) are given.

Considering these results and the individual layer thicknesses of the specimens, the element length is set to 0.25 mm for specimens 1 and 4. For specimens 2 and 3 an element length of 0.2 mm is used. Both values refer to the horizontal edge length of the element.

For the vertical element length, the horizontal length is adopted if possible or the layer thickness is used.

Table 3. Overview of wavelengths for the excited wave modes.

Material	Frequency kHz	S_0 Wavelength mm	A_0 Wavelength mm	Δx_{\max} mm
Aluminum	200	26.99	6.568	0.33
	250	21.58	5.787	0.29
	300	17.98	5.206	0.26
Steel-Film Adhesive	200	25.14	6.64	0.33
	250	19.96	5.791	0.29
	300	15.96	5.174	0.26
Aluminum-GFRP	200	26.60	8.308	0.42
	250	21.2	7.026	0.35
	300	17.44	6.122	0.31
GLARE 3-3/2-0.4	200	25.5	7.032	0.35
	250	20.38	5.964	0.30
	300	16.95	5.191	0.26

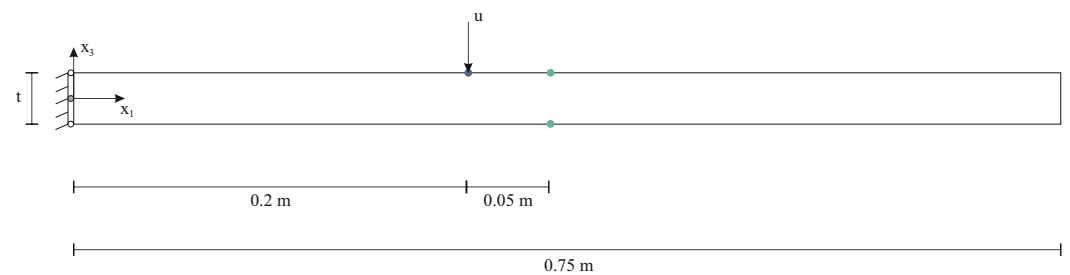


Figure 2. Graphical representation of the numerical model and its boundary conditions as described in Section 3.1.

3.2. Results From the Numerical Simulation

The numerical simulations provide, on the one hand, the dispersion relations and, on the other hand, the time signals representing the wave propagation in the different specimen setups.

The dispersion relations hold information about the occurring wavelengths, wave numbers, group velocities, and phase velocities. They also show at which frequencies higher order modes are excited and in which frequency range only the fundamental modes occur. As indicated in Section 2.1, in addition to the fundamental modes, the possible influence of modes of higher order on the phase evaluation procedure is to be taken into account.

As can be seen in Figure 3a, modes of higher order do occur for the aluminum-GFRP laminate from approx. 270 kHz and for the steel-film adhesive laminate at 180 kHz, as shown in Figure 3b. Consequently, within the range of the three chosen excitation frequencies, in these two laminates modes of higher order will be excited. These additional modes will appear as additional oscillations in the time signals. Hence, it needs to be evaluated in what way these modes will be present in the APDS. In aluminum and the GLARE 3-3/2-0.4-laminate, only the fundamental waves modes are excited within the chosen excitation frequency range as shown in Figure A1a (aluminum) and in Figure A1b (GLARE 3-3/2-0.4) in the Appendix A. In the Figures in the Appendix A, the frequency range reaches up to 600 kHz showing the first mode of higher order for GLARE 3-3/2-0.4 and the two fundamental modes for aluminum. Therefore, these plate and laminate setups serve as the fundamental mode representation because regarding their stiffness properties, no modes of higher order occur yet under the chosen excitation.

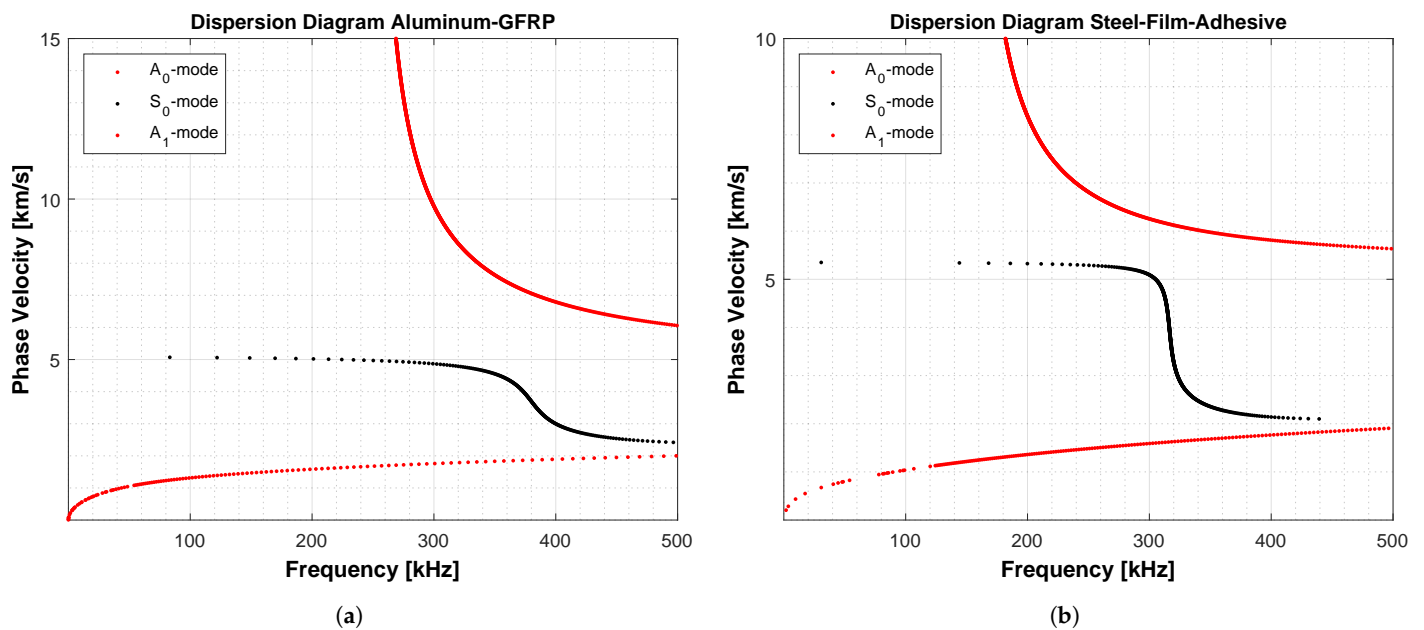


Figure 3. Dispersion diagrams of the phase velocity for the laminates which show modes of higher order in the chosen frequency range. (a) The dispersion diagram for the phase velocities in the aluminum-GFRP laminate indicating a cut-off frequency of higher order modes at approx. 270 kHz. (b) The dispersion diagram for the phase velocities in the steel-film adhesive laminate indicating a cut-off frequency of higher order modes at approx. 180 kHz.

The numerical simulation provides time signals for all four material settings. A pair of time signals per excitation frequency per specimen represents the oscillations on the structural top and bottom surface. When examining these simulated time signals, a signal grouping according to the time course properties will facilitate the later interpretation of the derived APDS. Therefore, all time signal pairs are compared with respect to the occurring wave packages. Referring to the 2D-numerical model, the time signals can be separated into the in-plane signal courses and the out-of-plane signal courses. Because in this work the experimental method is to detect the out-of-plane wave component, in the following the out-of-plane time signal is considered, and the in-plane part is neglected. Following this, two characteristic signal groups can be described.

Signal Group 1: The time signals of the upper and lower surface show two areas. The first can be identified as a low-amplitude S₀-mode shifted by π , which passes directly into the in-phase A₀-mode of a significantly higher amplitude. No oscillations after the A₀-mode occur, the time signals are in phase and show congruence in the representation (c.p. Figure 4a). Regarding the other time signal pairs of the same characteristics, it can be observed that the amplitude of the S₀-mode increases with excitation frequency for all material settings and is lowest in aluminum in comparison to e.g., the steel-film adhesive.

Signal Group 2: The time signals in this group show three different areas. The first can again be identified as a low-amplitude S₀-mode with time signals shifted by π , which also passes directly into the in-phase A₀-mode. However, in contrast to signal group 1, the A₀-mode goes directly into a phase-shifted oscillation. This oscillation shows amplitudes comparable to the S₀-mode identified at the time signals' beginnings (c.p. Figure 4b) but increases with the excitation frequency. Hence, a third wave package exists.

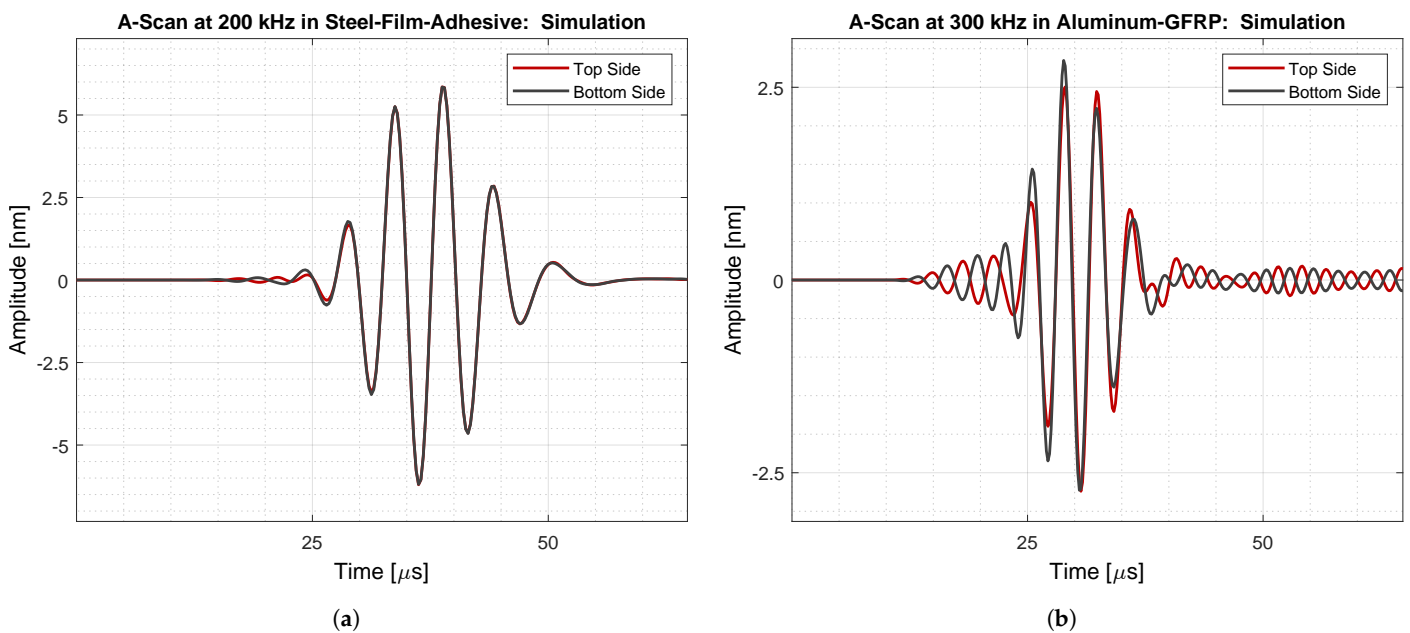


Figure 4. Simulated out-of-plane time signals for different laminates at different frequencies showing the division into areas of different oscillations. (a) Out-of-plane time signals of the wave propagation in the steel-film adhesive at 200 kHz assigned to signal group 1. (b) Out-of-plane time signals of the wave propagation in aluminum-GFRP at 300 kHz as example for signal group 2.

The third wave packages appear in some time signal pairs due to the excitation of higher-order wave modes in the specific specimen at the specific excitation frequency. As shown in Figure 3a,b, the dispersion relations show modes of higher order for the steel-film adhesive laminate and the aluminum-GFRP plate below 300 kHz. Concretely, this means higher-order wave modes in the steel-film adhesive at 200 kHz, at 250 kHz, and at 300 kHz as well as higher-order modes in the aluminum-GFRP laminate at 300 kHz. Wave modes of higher order hence lead to additional oscillations in the time signals. The time signals of all excited frequencies for aluminum and GLARE 3-3/2-0.4 without higher order modes can all be assigned to signal group 1.

Regarding their time course, all time signals for each specimen type can be divided into these two presented groups as listed in Table 4, depending on the selected frequency. Signal group 2 consists of just four different time signal series, which differ at two entries from the dispersion relations (steel-film adhesive at 200 kHz and aluminum-GFRP at 250 kHz). This classification is based on the comparison of oscillations to the mode with the highest amplitude of the presumed A_0 -mode. Hence, possibly smaller oscillations are neglected because they are too small in comparison with the highest amplitude. It must be taken into account that they may be present in the numerical results. For example, a higher-order S_1 -mode is expected in the steel-film adhesive at 200 kHz, but does not show oscillations in the time signal. The assignment in Table 4 is hence marked with an asterisk to make clear that it differs from the expected assignment to signal group 1. In contrast to this, in aluminum-GFRP at 250 kHz, no modes of higher order are expected yet, referring to the dispersion diagram in Figure 3a, but low-amplitude oscillations appear and lead to an assignment to signal group 2. This differs from the expectation when compared to the dispersion diagrams.

Table 4. Overview of the time signal assignment in signal group 1 and signal group 2.

Material Frequency [kHz]	Aluminum	Steel-Film Adhesive	Aluminum- GFRP	GLARE 3-3/2-0.4
200	1	1 *	1	1
250	1	2	2	1
300	1	2	2	1

* The occurrence of a mode of higher order is expected in this time signal referring to the dispersion diagram in Figure 3b. But since there is no mode of higher order visible, the time signal is assigned to signal group 1.

3.3. Evaluation of the Absolute Phase Difference Spectra

In the following, the two introduced methods are applied to the numerically obtained time signals and the APDS are determined. To simplify the later interpretation, the phase angles in the range of the excitation signals' bandwidth are considered. The main focus thereby lies on the center frequency itself. The temporal correspondence of the wave modes in the time domain and in the frequency domain of the APDS is also inspected. Regarding the time signal groups as presented in Section 3.2, it is examined whether this classification can be adopted for the derived APDS.

The Oscillation Phase Relation Obtained by the APDS-CWT

In the description of the APDS-CWT, the sequence regarding material and excitation frequency from Table 3 is kept, starting with the consideration of the time signals of the aluminum specimen.

The APDS-CWT for aluminum for all three frequencies (c.p. Figure 5a,b show the same pattern). At the beginning of the time segment in the APDS-CWT, a range of a π -shifted phase difference can be identified. The rest of the APDS-CWT shows no phase difference indicating that the in-phase A_0 -mode is identified. An increase of the center frequency of the time signals is accompanied with an increase of the π -shifted range in the APDS, as shown by a comparison of Figure 5a,b. This can be explained by the amount of periods of the S_0 -mode, which increases with the signals' center frequency. The fewer periods appear in a mode, the more difficult it is to identify it by the APDS due to time resolution issues. All three APDS-CWT of aluminum are assigned to signal group 1 (c.p. Table 5).

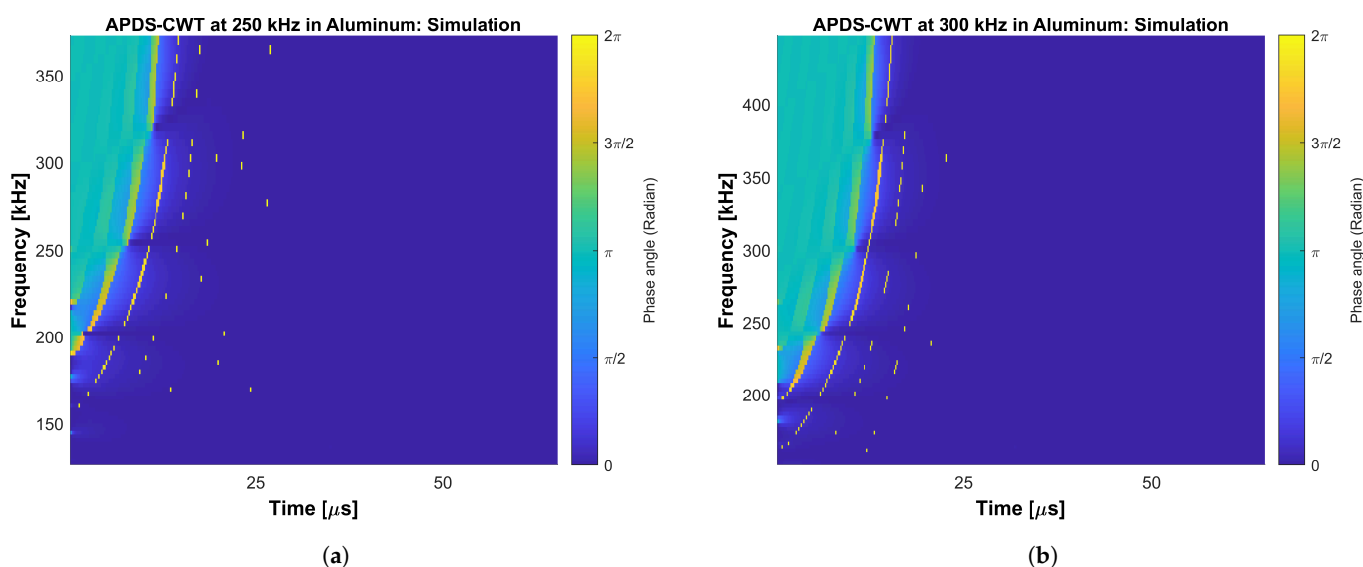


Figure 5. The APDS-CWT of the aluminum plate: the increase of the extension of the π -shifted area with increase of the time signal center frequency can be identified. (a) APDS-CWT of the Aluminum plate at 250 kHz. (b) APDS-CWT of the Aluminum plate at 300 kHz.

In the steel-film adhesive, the APDS-CWT show three areas along the time axes for the given frequencies. The first area describes a π -shift in the phase angle which corresponds to the S_0 -mode. This range is followed by an area without a phase shift corresponding to the A_0 -mode. In contrast to the APDS of signal group 1, the third area appears showing a shift by π . As the excitation frequency increases, this third area increases in frequency range and time, as illustrated for steel-film adhesive at 200 kHz in Figure 6a and for 300 kHz in the Appendix A in Figure A2a. Due to the tripartite division, all APDS-CWT for the steel adhesive are marked as signal group 2 in Table 5. This corresponds to the expected behavior due to the excitation of higher order modes for all excitation frequencies in steel-film adhesive.

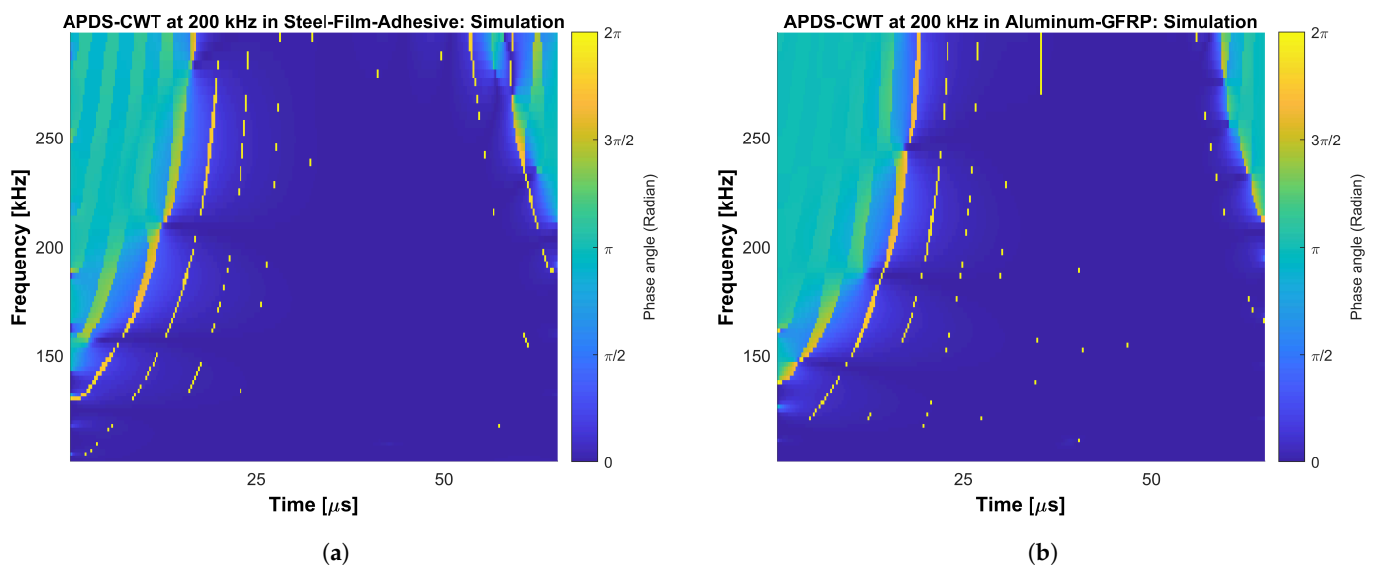


Figure 6. The APDS of the aluminum-GFRP plate and the steel-film adhesive plate at 200 kHz: the same characteristics as expected for signal group 2 can be identified. (a) APDS-CWT of the steel-film adhesive plate at 200 kHz. (b) APDS-CWT of the aluminum-GFRP plate at 200 kHz.

The APDS-CWT for the aluminum-GFRP laminate show qualitatively the same patterns as observed in the steel-film adhesive for all used excitation frequencies (c.p. Figure 6a,b at 200 kHz as well as Figure A2a,b at 300 kHz in the Appendix A). Therefore, the signals are assigned to signal group 2 in Table 5. The behavior at 200 kHz in aluminum-GFRP deviates from the expected signal group 1. Hence, in Table 5 the entry for aluminum-GFRP at 200 kHz is marked with an asterisk.

In the GLARE 3-3/2-0.4 laminate, no higher order modes are excited within the given frequency range as indicated in the dispersion diagram shown in Figure A1b in the Appendix A. Hence, a similarity between the APDS-CWT in aluminum and GLARE is expected as in the aluminum plate no modes of higher order do occur. This observation still applies for the time signals at 200 kHz and 250 kHz for GLARE in comparison with aluminum (c.p. Figure A3a in the Appendix A with Figure 5a). In contrast to this, the behavior at 300 kHz is different. The comparison between the APDS-CWT for GLARE in Figure A3b in the Appendix A with the APDS-CWT in aluminum in Figure 5b illustrates that the APDS-CWT in GLARE shows the pattern of signal group 2 with an additional area with a π -shift at the end of the time axes. This was not expected because the dispersion relation for GLARE does not yet indicate higher-order modes at the excitation frequencies. A closer look at the time signals for GLARE at 300 kHz indicates a very low-amplitude π -shifted oscillation following the A_0 -mode. The amplitude is in the range of 10×10^{-11} m/s and therefore orders of magnitude smaller than the A_0 -mode. This oscillation can be explained by effects caused by the numerical model's boundary conditions. Due to the appearance in the APDS-CWT and the tripartite division, the APDS at 300 kHz for GLARE

belongs to signal group 2. It is marked in the Table 5 with an asterisk because it differs from the time signal group assignment in Table 4.

Table 5. Overview of the APDS-CWT assignment into signal group 1 and signal group 2. Positions that differ from the assignments in Table 4 are marked with an asterisk .

Material Frequency [kHz]	Aluminum	Steel-Film Adhesive	Aluminum-GFRP	GLARE 3-3/2-0.4
200	1	2 *	2 *	1
250	1	2	2	1
300	1	2	2	2 *

* Deviation from the signal group assignments in Table 4.

Finally, the assignments for steel-film adhesive at 200 kHz as well as aluminum-GFRP at 200 kHz and GLARE for 300 kHz differ from the time signal groups in Table 4 and are marked with an asterisk. They have in common that they all show the signal group 2 characteristic, i.e., an area with a shift by π . This is identified by the method and was not discovered in the time signals. For the steel-film adhesive at 200 kHz, oscillations of a higher-order mode can be expected, referring to the dispersion relation in Figure 3b. In aluminum-GFRP at 200 kHz and in GLARE at 300 kHz, numerical effects in the time signals cause oscillation that are identified by the method.

The Oscillation Phase Relation Obtained by the APDS-STFT

In this section, the patterns of the APDS-STFT are evaluated. The time signals in Tables 4 and 5 are classified in correspondence to the occurrence of higher-order modes or their absence. Hence, two different patterns for the APDS-STFT are expected as well. The thematic order of specimen introduced in Table 3 is resumed, starting with aluminum.

At 200 kHz, the APDS-STFT for aluminum does not identify the π -shifted S_0 -mode as seen in the time signal course of signal group 1 (c.p. Figure 7a). Along the entire time scale and all frequencies, the APDS-STFT determines a phase angle difference of 0, resp. nearly 0. Except for thin lines of 2π , which are identical to a phase angle difference of 0, no phase shift is detected. Because this is a new unexpected behavior that does not fit in any of the two signal groups, it is marked in the Table 6 with two asterisks. In contrast to this, the APDS-STFT at 250 kHz and at 300 kHz, both show the same pattern among themselves. At the beginning of the time scale, a shift of π can be identified, whereas the rest of the two APDS-STFT does not show any phase shift. Hence, the two APDS-STFT are assigned to signal group 1 as listed in Table 6. As they contain two areas of different phase angles, the similarity to the occurrence of wave modes in the time signals is sensible.

Table 6. Overview of the APDS-STFT assignment into signal group 1 and signal group 2. Positions that differ from the assignments in Table 4 are marked with an asterisk.

Material Frequency [kHz]	Aluminum	Steel-film adhesive	Aluminum-GFRP	GLARE 3-3/2-0.4
200	**	1	1	1
250	1	2	1 *	1
300	1	2	2	1

* Deviation from the signal group assignments in Table 4. ** Signal behaviour that can be assigned neither to signal group 1 nor to signal group 2.

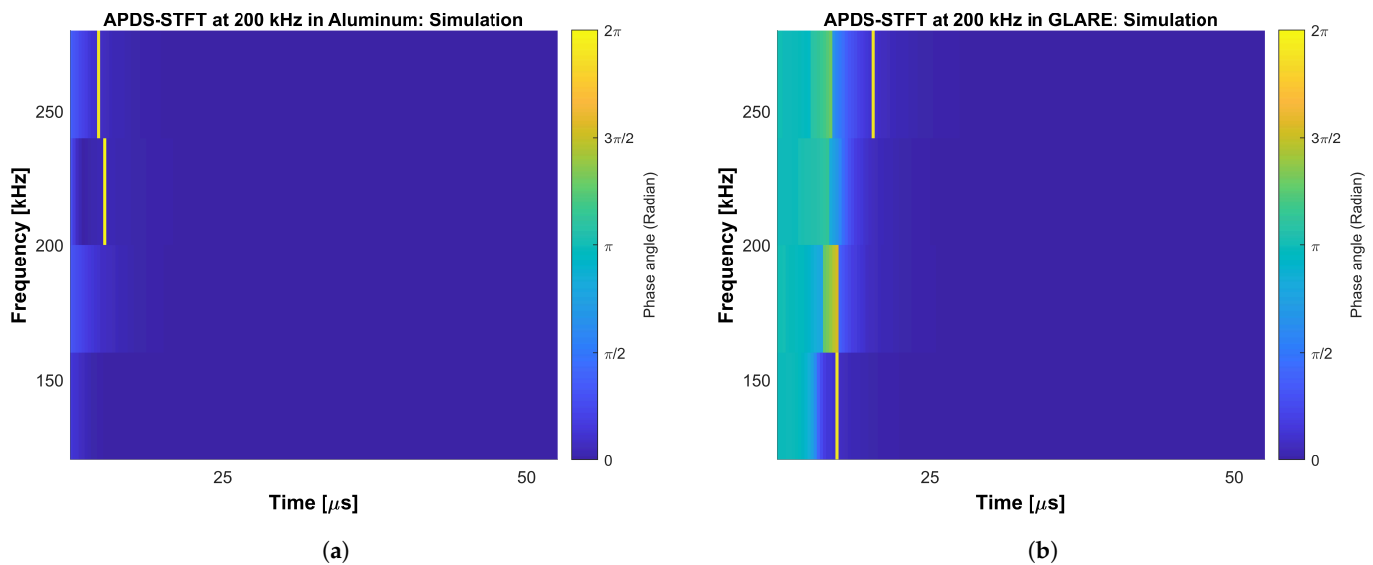


Figure 7. The APDS-STFT of the aluminum plate and the GLARE 3-3/2-0.4 plate at 200 kHz: the phase-shift in S_0 -mode is identified whereas the rest of the spectra shows no phase shift in correspondence with the time signals. (a) APDS-STFT of the Aluminum plate at 200 kHz. (b) APDS-STFT of the GLARE 3-3/2-0.4 plate at 200 kHz.

Whereas the APDS-STFT in steel-film adhesive at 200 kHz shows a pattern corresponding to signal group 1, the behavior at 250 kHz and 300 kHz differs from it. At 250 kHz, areas with a phase shift by π at the beginning and the end of the time scale appear. This tripartite is similar to the APDS-CWT described previously and corresponds to the wave modes' appearance in the time domain. The third area with a shift by π expands its reach over all frequencies for 300 kHz (c.p. Figure 8a). This increase of the π -shifted area in the APDS-STFT with increase of the excitation frequency corresponds to the signal behavior in the time domain, because in the time signals the phase-shifted area expands from 250 kHz to 300 kHz. Hence, these two APDS-STFT of the steel laminate are assigned to signal group 2 (c.p. Table 6).

In the APDS-STFT for aluminum-GFRP at 200 kHz, a range with a phase angle of π occurs in the beginning of the time scale, followed by an area without any phase shift. This pattern corresponds to signal group 1. At 250 kHz, the APDS-STFT of aluminum-GFRP shows some lines with phase angles close to 2π at the end of the time course and otherwise no phase shift. Accordingly, it is considered to be signal group 1 behavior. In the corresponding time signals, the two identified wave modes are followed by a third wave package. This is not identified by the APDS-STFT and therefore leads to the assignment in signal group 1. Because this differs from the expectation, it is marked with an asterisk in Table 6. The APDS-STFT at 300 kHz (c.p. Figure 8b) shows the same pattern as for the steel-film adhesive plate at the same frequency, i.e., three areas in the APDS-STFT with a significant phase-shift from π to 0 and to π at the end of the time scale. Hence, the APDS-STFT of aluminum-GFRP at 300 kHz is assigned to signal group 2.

For the GLARE 3-3/2-0.4-laminate, the pattern of the APDS-STFT can be easily classified. All three APDS-STFT start at the beginning of the time axes with a phase shift of π whose extension increases with increase of the excitation frequency. This area is followed by a phase angle of 0. All three APDS-STFT of GLARE 3-3/2-0.4 hence correspond to signal group 1 in Table 6. The pattern is illustrated by Figure 7b.

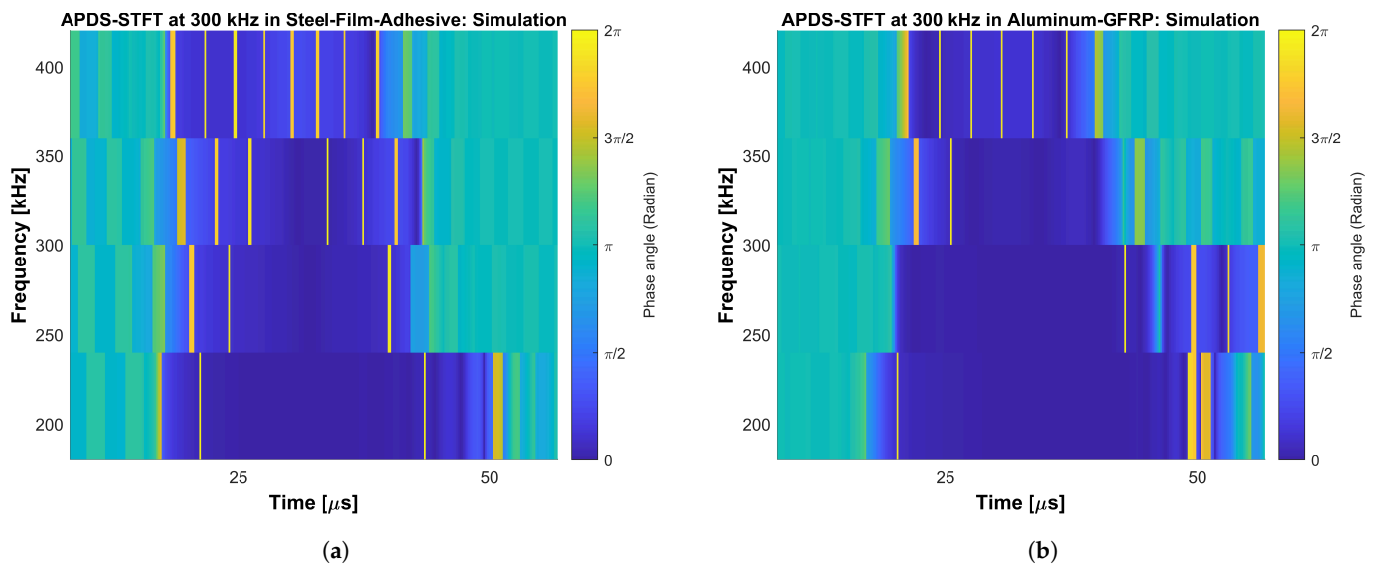


Figure 8. The APDS-STFT of the steel-film adhesive plate and the aluminum-GFRP plate at 300 kHz: the S_0 -mode is identified (blue area in the middle) and an area of a phase shift of π shows at the end of the time axes. (a) APDS-STFT of the steel-film adhesive plate at 300 kHz. (b) APDS-STFT of the aluminum-GFRP plate at 300 kHz.

The time signals at the given excitation frequencies in the aluminum plate and GLARE 3-3/2-0.4 do not show higher-order modes. Hence, they are assigned to the same signal group (c.p. Table 4). Therefore, their APDS-STFT are expected to have the same patterns among themselves. In the overview given in Table 6, this is the case, except for the time signals in aluminum at 200 kHz. Aluminum-GFRP at 250 kHz is also an exception of the expected classification because the APDS-STFT provides the pattern of signal group 1 instead of signal group 2. This does not correspond to the identified time signal course. However, it meets the expectation from the dispersion diagram in Figure 3a, indicating no modes of higher order yet and hence, expecting signal group 1. The two deviations can be explained by the resolution in the frequency domain of the APDS-STFT. Lower excitation frequencies generally lead to smaller areas of the π -shifted area. This corresponds to a lower extent of the S_0 -mode in the time domain. There is the risk that a smaller amount of oscillation periods in the time signals together with a poor time-frequency resolution in the evaluation method can lead to not identifying a certain wave mode. It is concluded that for aluminum at 200 kHz, the time-frequency resolution is too low to identify the S_0 -mode. This is confirmed by the fact that the mode is detected in the APDS-CWT as listed in Table 5. The CWT has a better time-frequency resolution behavior compared to the STFT, which reinforces the explanation accordingly. Additionally, increasing excitation frequencies in the APDS-STFT leads to narrow lines with phase angles of almost 2π . These angle differences equal 0 and can hence be neglected.

4. Results of the Application to Experimental Data

In this section, both introduced APDS methods are applied to experimentally captured time signals of the previously chosen excitation frequencies. The experimental procedure is carried out on the aluminum-GFRP plate presented in Section 2.1 as a representation of an FML.

4.1. Experimental Setup and Procedure

The aim of the experiment is to detect structural wave propagation in an FML on congruent measurement points on the two surfaces of the structure. For the implementation, a PSV-400 laser Doppler vibrometer (LDV) (Polytec GmbH, Waldbronn, Germany) is used for the detection of the oscillation on the specimens' surface. Because the one-dimensional

LDV detects the out-of-plane component via structural movement in relation to the laser beam, the signal evaluation is focused on the oscillations' out-of-plane component as also done for the numerical obtained data. A five-cycle Hanning-windowed sine burst is used as excitation signal with an output voltage of 1.5 V. It is generated by the LDV's internal signal generator and amplified by 50 times by a Falcon system voltage amplifier 300-WMA before being applied to the PZT-ceramic actuator (material: PIC255, diameter: 16 mm, thickness: 0.2 mm, type: PRYY-1126, PI Ceramic GmbH, Lederhose, Germany). For the structural excitation of the specimen, the PZT ceramic lies in the center of the structure. It is adhesively bonded by using commercial super glue. A perfect bonding is assumed. The center frequencies of the sine burst excitation signals are 200 kHz, 250 kHz and 300 kHz. The signal recording time length is adjusted in such a way that reflections from the specimen's edges are not captured. Hence, the signal recording length is chosen to be 65 μ s. The sample frequency is set to 5.12 MHz. The internal data processing of the LDV enables the compensation of angular errors of the laser beam, and thus provides the vibration component perpendicular to the structural surface. A measurement point is chosen on the upper and lower surface of the specimen. In order to be able to compare the oscillation phase, it must be ensured that congruent measurements can be undertaken on both surfaces of a structure. Equal signals that are shifted in time show differences in the phase spectrum [5]. Hence, the phase spectrum is sensitive to errors caused by time shifts that occur due to positioning errors. Therefore, the measurement point is precisely measured in relation to the plates' edges. It is marked on the retroreflective foil on the top and bottom surfaces so that it can be precisely targeted with the laser measuring beam. The measurement point is chosen in a distance of 50 mm from the actuator to avoid near field effects. Attached positioning aids on the table ensure a stable reproducible positioning of the specimen because the plate is turned from one surface to the other after a measurement run is performed.

The sketch in Figure 9 illustrates the concept of the experimental setup. The bilateral measurement is indicated via the two drawn LDV heads. The red lines illustrate the laser beam hitting the structure at congruent measurement points detecting the phase of the out-of-plane oscillation.

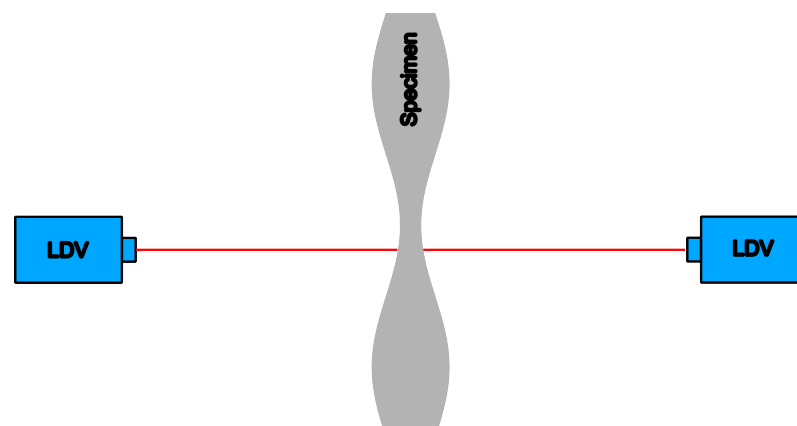


Figure 9. A sketch of the experimental setup illustrates to congruence of the measurement points on the top and bottom surface of a specimen.

4.2. Comparison of the APDS-CWT and APDS-STFT Derived from Measured Oscillation Time Signals

In the following, the APDS methods will be applied to experimental data. It is important to investigate the extent to which experimental data deviate from numerical data and whether these peculiarities make the interpretation of the spectra more difficult. Figure 10 illustrates exemplary the courses of the time signals of the performed LDV-measurements at 200 kHz. They exhibit a high congruence (c.p. also Figure 4a at 250 kHz and Figure 4b at 300 kHz in the Appendix A).

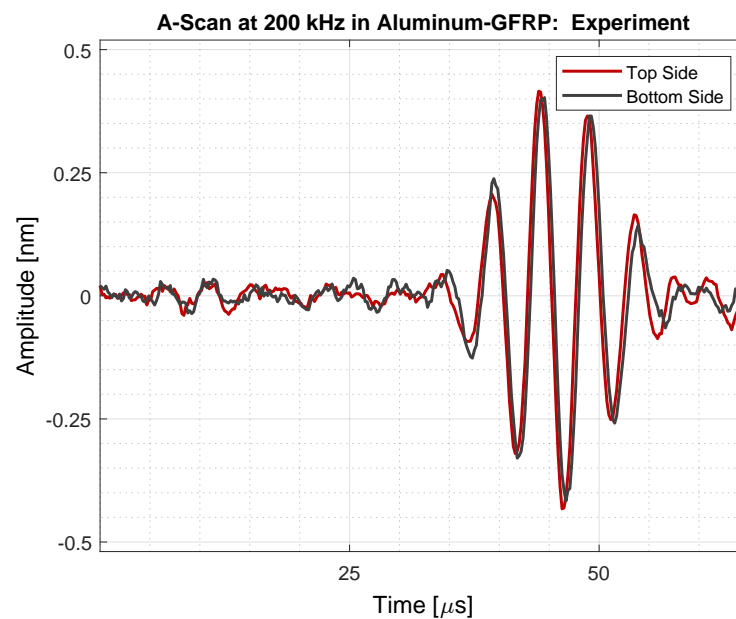


Figure 10. The captured time signals in the aluminum-GFRP plate on the top and bottom surface at 200 kHz.

Slight shifts in the signal courses can be explained by measurement uncertainty. A wave mode, which is in phase, appears at approx. $10 \mu\text{s}$ in the time signals of all scans. The following wave package is also in phase and shows higher amplitudes. It corresponds to the A_0 -mode. Additionally, in Figure 4b after the A_0 -mode, a range appears that shows oscillations shifted by π . Corresponding phase shifts in the APDS can therefore be expected. Because of the good agreement, all three measurements of aluminum-GFRP are evaluated by the APDS methods in the following.

A closer look at the APDS-CWT and APDS-STFT at 200 kHz is taken as presented in Figure 11a (APDS-CWT) and Figure 11b (APDS-STFT).

Both the APDS-STFT and the APDS-CWT identify the phase ranges along the time axes. Slight narrow areas of phase shifts by approx. 2π can be found in both APDS. They can on the one hand be explained by measurement uncertainty and noise. On the other hand, a shift by approx. 2π is equivalent to a phase of 0. Thus, the APDS both show no significant range of a phase angle other than 0. This corresponds to the congruent time scans shown in Figure 10. Accordingly, the characteristics of phase shift free spectra can be seen clearly. In the measurement setup, neither the specimen nor the LDV were moved. Hence, for the captured time signals at 250 kHz and at 300 kHz, the same congruence emerges (c.p. Figure A4a,b in the Appendix A). For both frequencies, the captured time signals contain two wave packages in phase. They are identified in all spectra as regions with no phase angle difference (c.p. Figure A5a,b at 250 kHz and Figure A6a,b at 300 kHz in the Appendix A). All spectra are again crossed by narrow lines that show an angle of approx. 2π . An increase of noise in the time signal can be observed when the excitation frequency also increases. These noise effects also occur in both spectra as small regions of phase angle discontinuities. In conclusion, the in-phase time signals for all frequencies are qualitatively represented in all the spectra, more specifically in the APDS-CWT.

The application of the APDS methods to the experimental data leads to specific challenges. For example, the congruence of the measurement points is crucial in the experiments, because small shifts in the position might lead to the detection of a different phase position of the oscillation than if complete congruence is achieved. In the APDS of both types, measurement noise in the time signals is detected by the methods. This is explained by the fact that they operate independently from the signals' magnitude. Additionally, the APDS-CWT and the APDS-STFT show smooth transitions between phases. Hence, accurate localization in the time domain is difficult and can only be done qualitatively. As described

previously, the APDS-CWT and the APDS-STFT for the experimental data lead to in-phase areas which are crisscrossed by thin lines of phase angle difference of approx. 2π . These lines do not have a physical meaning because they correspond to a phase angle difference of 0. An influence of measurement noise is to be expected and profound filtering needs to be discussed for the simplified application of the APDS methods.

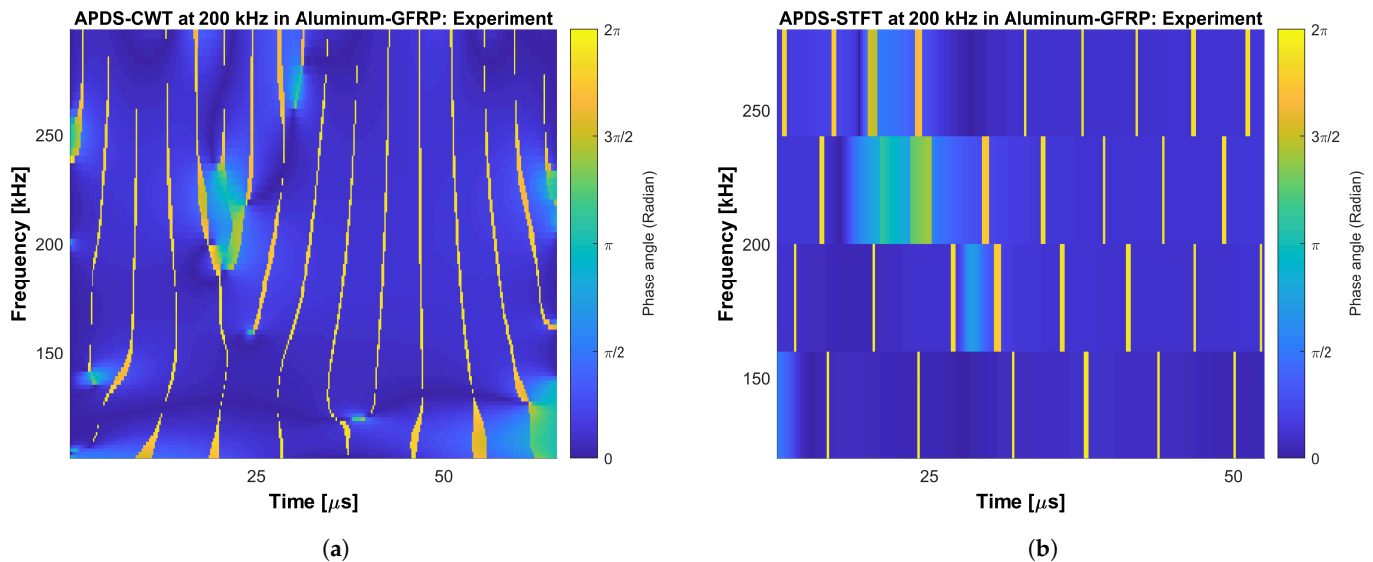


Figure 11. The APDS-CWT and APDS-STFT of the aluminum-GFRP plate at 200 kHz with no extended phase shifts corresponding to the associated time signals. (a) APDS-CWT of the aluminum-GFRP plate at 200 kHz. (b) APDS-STFT of the aluminum-GFRP plate at 200 kHz.

5. Discussion

In this section, the APDS-CWT and the APDS-STFT are evaluated from two perspectives. First, the relationship between the time domain and the frequency domain is described and discussed. Secondly, the APDS-CWT and APDS-STFT methods are evaluated with respect to their time-frequency resolution properties.

5.1. The Relationship Between the Signals in the Time Domain and the Frequency Domain Using the Example of APDS-CWT

In order to enable an evaluation of the two presented methods, it is particularly crucial to consider how well the transformation from the time domain to the frequency domain of the APDS can be performed. This forms the basis for the application of the developed methods for evaluation of oscillation signals.

In Figure 12, the time signals and the APDS-CWT of the wave propagation at 250 kHz in aluminum are juxtaposed. The S_0 -mode shows with a very low amplitude between approx. $10\ \mu\text{s}$ to $20\ \mu\text{s}$ in the course of the time signals. At the transition zones, i.e., at the beginning of the time axes in Figure 12, the APDS already detects a phase angle difference at particular frequencies before the S_0 -mode occurs in the time signals. When comparing the time signals in the range of the A_0 -mode, the APDS-CWT identifies the phase angle difference of 0. This suits the time course shown above. Hence, the comparison between the two representations lead to the conclusion that the relation between the occurring phases and the range in the time domain correspond qualitatively. This mismatch between phase angle identification and occurrence in the time course can be explained by the uncertainty principle. There are constraints regarding the resolution in time and frequency domain. It is concluded that a direct comparison between the time axes of the A-scans and the time axes of the APDS show transition zones from one phase angle area to the other. Hence, the APDS serve as qualitative tool for the estimation of the occurring phase relations. The assignment of the modes is possible nonetheless.

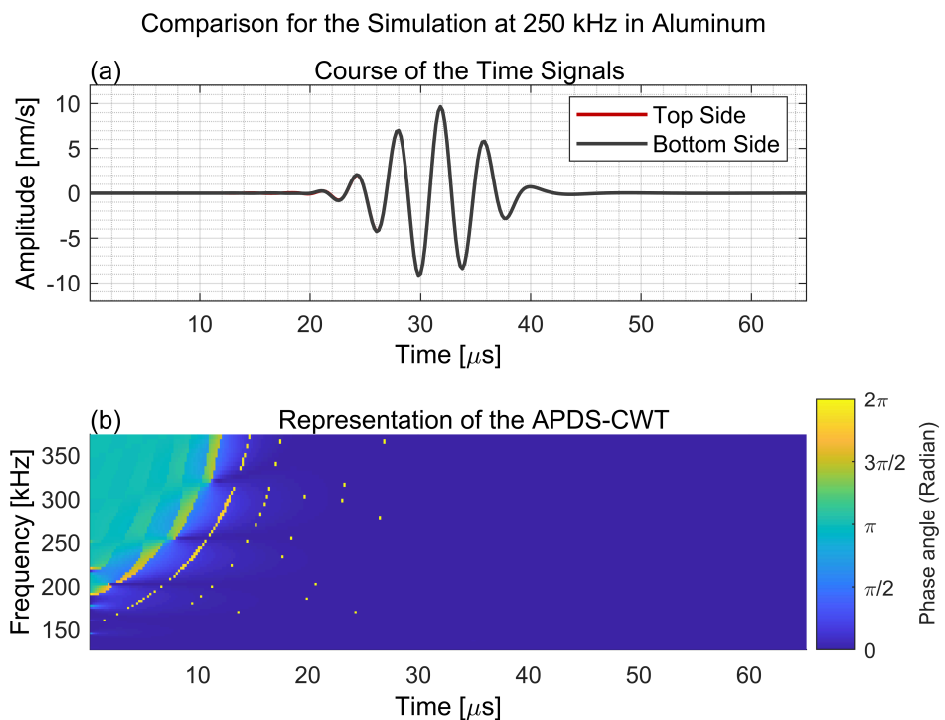


Figure 12. Juxtaposed time signals and the APDS-CWT in aluminum at 250 kHz. **(a)** Time domain: The course of the time signals. **(b)** Frequency domain: The APDS-CWT.

Additionally, it is noted that the expansion of the ranges of phase angle differences in the APDS-CWT is influenced by the course of the oscillations in the time signals and the amount of oscillation periods. An increase of oscillation periods in the S_0 -mode leads to an expansion of the area with phase shift in the APDS. As an example, the S_0 -mode in GLARE at 250 kHz in Figure 13a counts 3.5 cycles and the S_0 -mode in GLARE at 300 kHz in Figure 13b counts 4.5 cycles. Simultaneously, these low-amplitude oscillations show an increased amplitude from approx. 30 pm at 200 kHz up to a doubling to approx. 60 pm at 300 kHz.

This observation leads to the conclusion, that even low-amplitude oscillations are identified by the two methods independent from the oscillations' origin and independent from the oscillations' amplitude. Due to the mathematical properties of the transformation, the length of the time signals has a significant impact on the expansion of the π -shifted areas in the APDS. This observation especially applies to the APDS-STFT, as it is presented in this work due to the lower time-frequency resolution. Taking this into account, additional measurement deviations possibly lead to spectra of the APDS, which are not clearly interpretable and do not offer an unambiguous relationship between time and phase angle of a wave mode. This challenge corresponds to the descriptions in the literature, that phase spectra in general are prone to error because slight shifts in the time reference already causes a significant shift in the phase angle [5]. This effect can only slightly be eliminated by windowing the segments. Other approaches, like adjusting the overlap in the STFT, the amount of octaves in the CWT, the size of the time step in the time signals etc. can help to optimally design the transformation methods for the planned application.

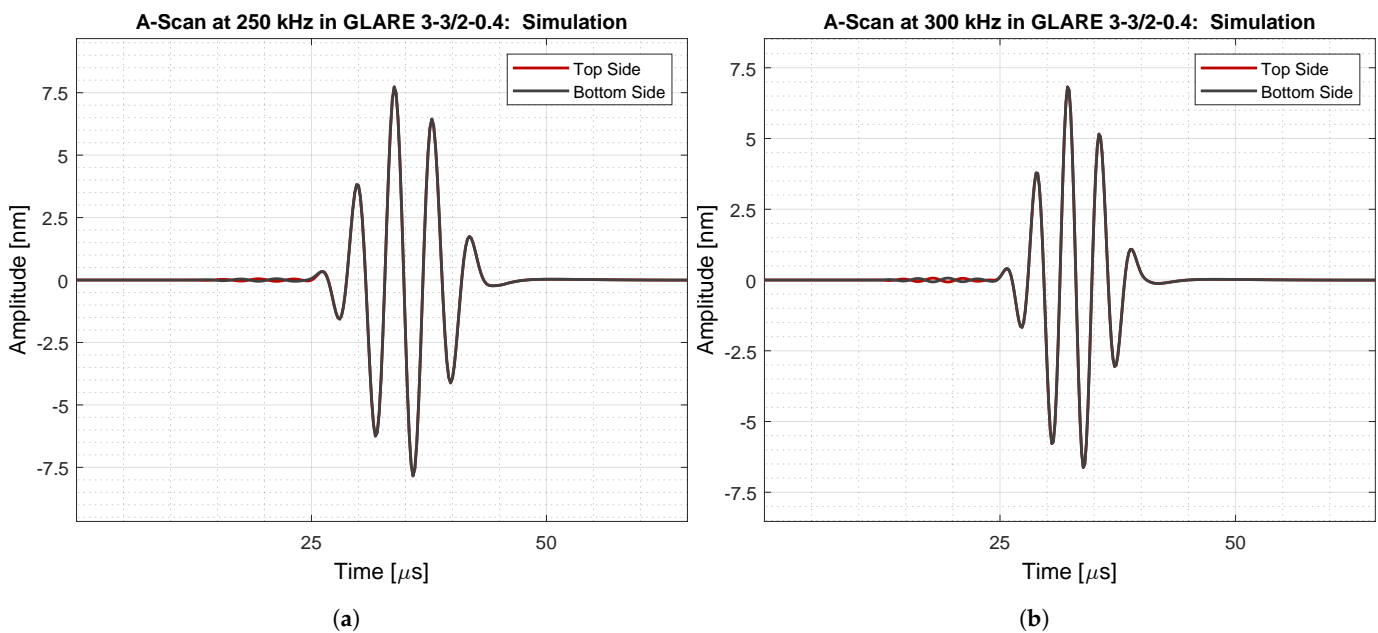


Figure 13. Comparison between the time signals in GLARE at different frequencies: the increase of the π -shifted area with increase of the time signal center frequency in the APDS in Figure A3a,b can be explained by the increase of oscillation periods in the time signals. (a) Time signals of the GLARE plate at 250 kHz. (b) Time signals of the GLARE plate at 300 kHz.

5.2. The Suitability of the Presented Methods for the Oscillation Phase Identification

Considering the task of evaluating the phase relation of oscillating multifrequent transient signals, the two presented methods show advantages and drawbacks. Both methods face the challenge of offering a sufficient resolution in the time domain as well as in the frequency domain. The resolution can be positively influenced by a sufficient small time step in the experimental recordings as well as in the simulated time signals, which will be of advantage for the APDS-CWT as well as for the APDS-STFT.

The APDS-CWT show the ranges of oscillation in phase and shifted by π . Regarding the APDS-CWT for some numerical data, i.e., steel-film adhesive at 300 kHz as shown in Figure A2a, the simulated time signals lead to in-phase areas which are crisscrossed by thin lines of higher phase angles. This is observed with an increase of the excitation frequency for the different plate setups and hence indicates to be frequency-dependent. A possible explanation is that the phase does not show a clean in-phase behavior due to slight numerical deviations in the time signals. In the APDS-CWT, the wider range of the shown phase angle differences are either 0 or π which corresponds to the wave modes identified in the course of the time signals. It can be seen that the extent of these areas in the APDS do not exactly correspond to the time axes in the time signals. This is due to the uncertainty created by the transformation process itself. The comparison between the APDS-CWT and the APDS-STFT confirms that the CWT offers a more exact resolution in the time and frequency domain. Referring to the signal group assignments in Tables 5 and 6, both methods show good agreement with the expected signal group behavior. Deviations from the group assignments occur for two APDS-STFT and three APDS-CWT. They can be explained by time-frequency resolution on the one hand for the STFT. On the other hand, additional oscillations caused by numerical effects are recognized especially by the APDS-CWT.

6. Conclusions

The main objective of this work is to answer the question of whether the oscillation phase relation on the upper and lower surface of plate-like structures made of FML under GUV wave propagation shows the same behavior as for GUV in metals or composites. Hence, two different frequency-time analysis methods are derived and used to evaluate

segment-wise time signals' oscillation phase angles. One method is based on the CWT and its IP information stored in the complex transformation parameters. The second method is based on the STFT. Phase difference spectra are extracted and compared regarding their capability of identifying the phase relation between in-phase wave modes and wave modes shifted by an angle of π . Properties like the uncertainty principle during transformation are taken into account because a good adjustment between the time axes allows a quick comparison of the gained spectra with the underlying time signals. During the evaluation, the main focus for the interpretation of the spectra lies on the excitation signal's bandwidth for both numerical and experimental data. Furthermore, the spectra cover the bandwidth of the excitation burst signal because these are the frequencies in which the wave modes physically appear on the excited structures. Higher and lower frequencies bands in the spectra can be interpreted as relicts of the transformation itself. It should be taken into account that numerical errors as well as effects of the boundary conditions in the simulation can lead to local variations in the phase and transition behavior between the phase π and 0. If not the absolute value of the difference is used, the order of the summands influences the later sign of the difference. Therefore, values of π and $-\pi$ can be interpreted the same as a phase shift of π and as an indication for local symmetric oscillation behavior. Due to numerical boundary conditions, low-amplitude oscillations can appear in the time signals. Their phase angle changes are present in the spectra of the numerical captured time signals. This shows that the spectra do not replace a critical interpretation of the results. This also applies for experimental errors such as positioning inaccuracies of the vibrometer's measuring laser. When interpreting the spectra, it needs to be taken into account that the APDS do not distinguish between signals of lower amplitude, i.e., structural vibration, measurement noise or numerical relicts. Because noise occurs randomly, its representation in the APDS is shown as random phase relations of slight extension.

This work proves that the oscillation phase relation between the upper and lower surface of FML shows the same wave propagation behavior of GUW in composites and metals resp. the GUW in FML form the same surface oscillation characteristics as the Lamb waves in metals or composites as presented in Section 1. The existence of Lamb waves in FML is thus proven. The CWT is found suitable to gain phase information by comparing oscillation signals from plates' upper and lower surfaces. The work also illustrates with the help of concrete examples that positioning accuracy is crucial in experiments. The effect of noise in the experimentally captured time signals significantly influences the APDS, because the evaluation procedures are magnitude-independent. Time signals being in phase can clearly be identified in all cases in the APDS. The narrow lines in the APDS-CWT and APDS-STFT which occur intensely when evaluating the experimental data (i.e., in Figure A6a,b) show phase jumps of approx. 2π and are caused by noise in the captured time signals. Profound filtering of the time signals as well as the implementation of thresholds in the methods will smooth the APDS representation of both methods. At this stage of the work, an estimation of the oscillation phase relation between transient time signals can be performed by using the concept of the APDS-STFT and a more detailed observation via the APDS-CWT. To gain a better adjustment between the points in time in the time domain and the points in time in the frequency-domain, it is recommended to set the STFT to the maximum possible overlap and then use, in the CWT, as many scales per octave as is feasible.

In future work, the optimization of the presented methods will be addressed. The APDS-CWT as well as the APDS-STFT will be adjusted in their settings until the best possible agreement between time domain and frequency domain is found. When applied to measured data, background noise and superimposing errors need to be taken into account. Because noise shows in the APDS as a small, discontinuous phase, postprocessing will help insmoothing the representation. Thresholds will be implemented as well to smooth the representation when noisy experimental data is used.

Author Contributions: Conceptualization, L.R.; methodology, L.R., N.R. and A.M.; software, L.R., N.R. and A.M.; validation, L.R., N.R., M.S. and R.L.; formal analysis, L.R. and N.R.; investigation, L.R. and N.R.; resources, L.R. and N.R.; data curation, L.R. and N.R.; writing—original draft preparation, L.R. and N.R.; writing—review and editing, L.R., N.R., M.S. and R.L.; visualization, L.R. and N.R.; supervision, N.R., M.S. and R.L.; project administration, M.S. and R.L.; funding acquisition, N.R., M.S. and R.L. All authors have read and agreed to the published version of the manuscript.

Funding: The authors expressly acknowledge the financial support for the research work on this article of the Research Unit 3022 “Ultrasonic Monitoring of Fibre Metal Laminates Using Integrated Sensors” (Project number: 418311604) by the German Research Foundation (Deutsche Forschungsgemeinschaft (DFG)). We also acknowledge support by the Open Access Publication Funds of Technische Universität Braunschweig.

Institutional Review Board Statement: Not applicable.

Informed Consent Statement: Not applicable.

Data Availability Statement: The raw data of the experiments can be requested from the authors.

Conflicts of Interest: The authors declare no conflict of interest. The funders had no role in the design of the study; in the collection, analyses, or interpretation of data; in the writing of the manuscript, or in the decision to publish the results.

Appendix A

The appendix gives an overview of the dispersion diagrams, which do not show modes of higher order within the chosen excitation frequency range, an overview of some APDS-CWT for numerically captured time signals and the experimental time signals, as well as their derived APDS-CWT and APDS-STFT.

Appendix A.1. Dispersion Diagrams for Aluminum and GLARE 3-3/2-0.4

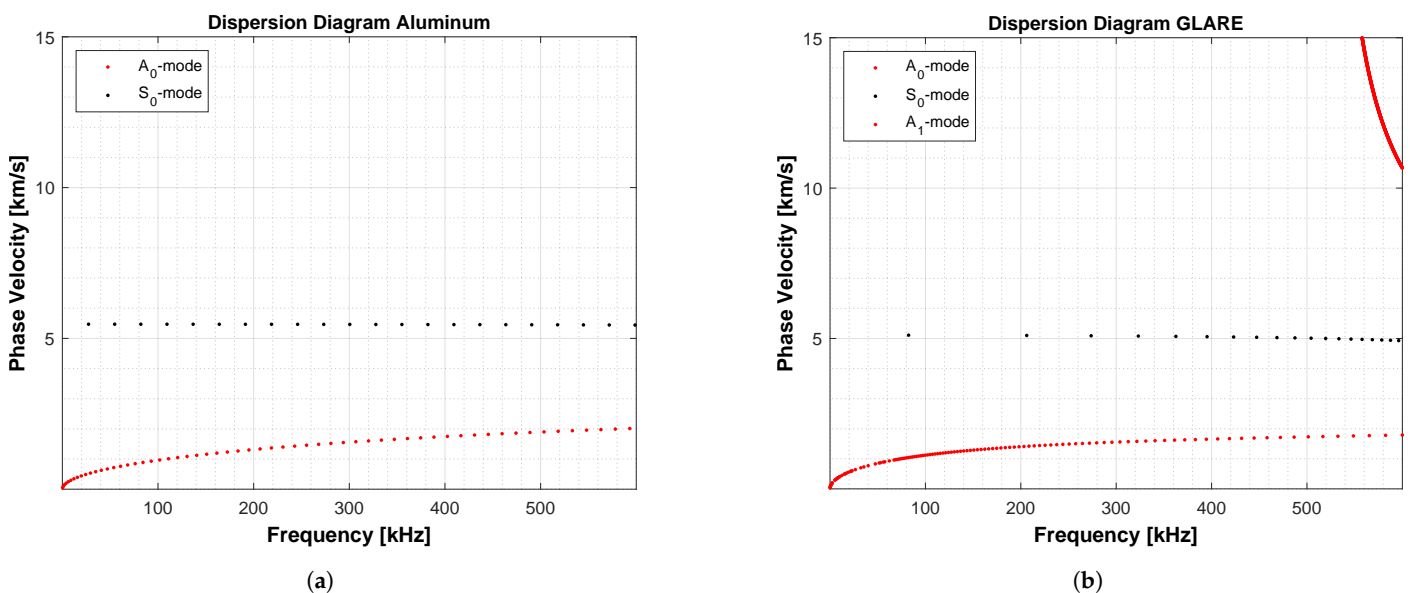


Figure A1. Dispersion diagrams of the phase velocity for the laminates which show no modes of higher order in the chosen frequency range. (a) The dispersion diagram for the phase velocities in the aluminum plate indicating no higher order modes under 300 kHz. (b) The dispersion diagram for the phase velocities in the GLARE 3-3/2-0.4 laminate indicating no higher order modes under 300 kHz.

Appendix A.2. APDS-CWT from Numerically Captured time Signals

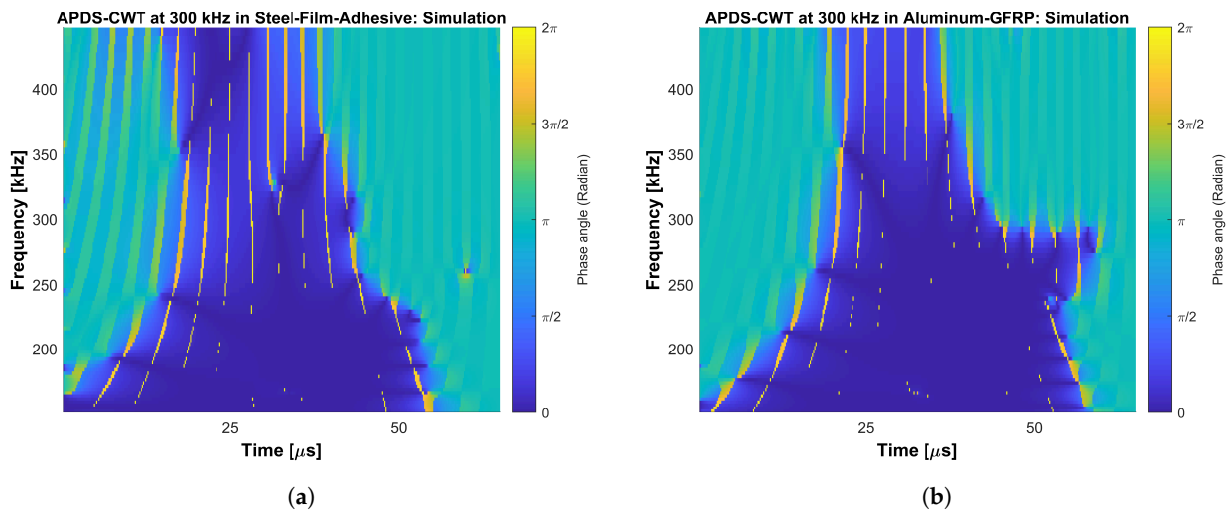


Figure A2. The APDS of the aluminum-GFRP plate and the steel-film adhesive plate: the same characteristics as expected for signal group 1 can be identified. (a) APDS-CWT of the steel-film adhesive plate at 300 kHz. (b) APDS-CWT of the aluminum-GFRP plate at 300 kHz.

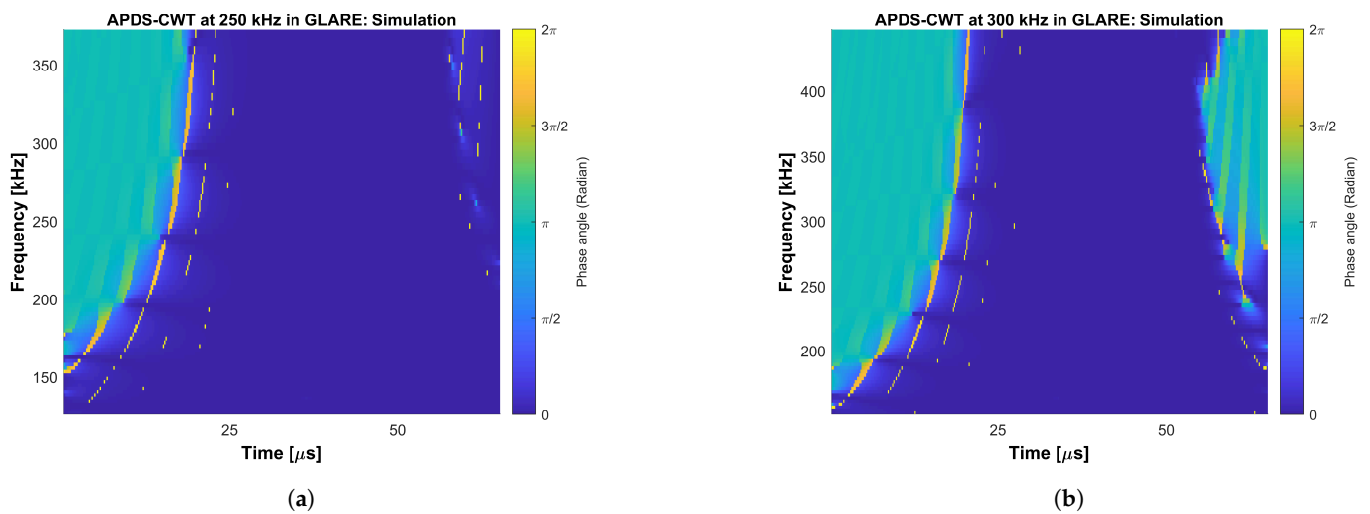


Figure A3. The APDS of the GLARE plate: the increase of the π -shifted area with increase of the time signal center frequency can be identified with an additional π -shift at 300 kHz. (a) APDS-CWT of the GLARE plate at 250 kHz. (b) APDS-CWT of the GLARE plate at 300 kHz.

Appendix A.3. Experimentally Captured Time Signals in Aluminum-GFRP at Different Excitation Frequencies in Reference to Table 3

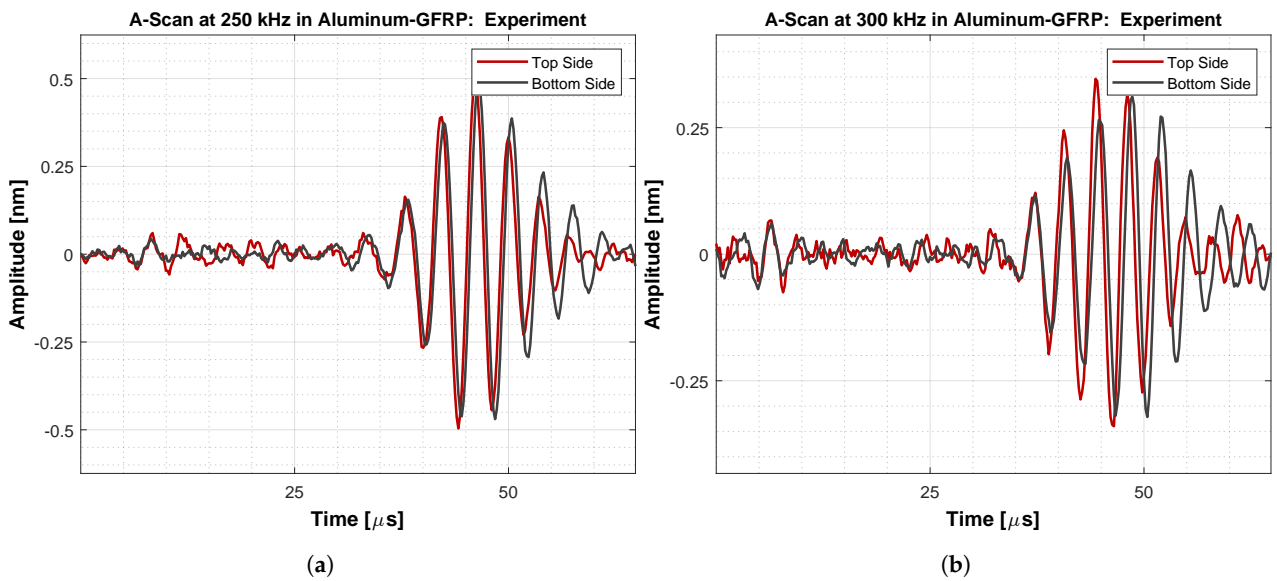


Figure A4. The captured time signals of the aluminum-GFRP plate at all three excitation frequencies showing good congruence between the top surface and bottom surface. (a) Time signals of the aluminum-GFRP plate at 250 kHz. (b) Time signals of the aluminum-GFRP plate at 300 kHz.

Appendix A.4. APDS from Experimentally Captured Time Signals

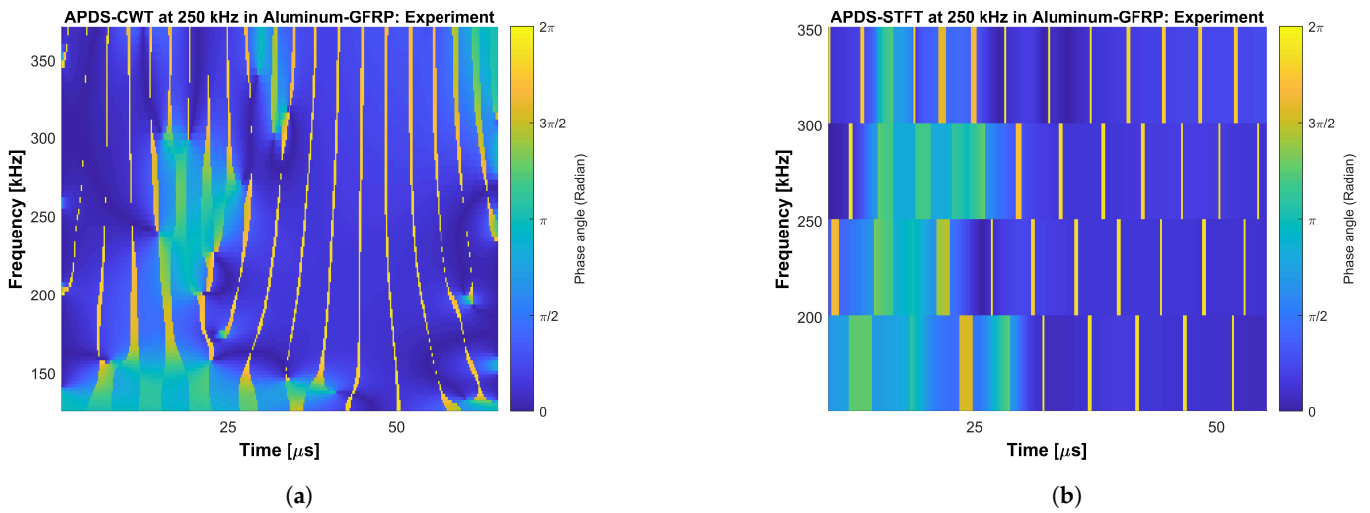


Figure A5. The APDS-CWT and APDS-STFT of the aluminum-GFRP plate at 250 kHz: the A_0 -mode is identified in the APDS-CWT whereas the APDS-STFT shows changes in the phase angle in the first half of the time axes. (a) APDS-CWT of the aluminum-GFRP plate at 250 kHz. (b) APDS-STFT of the aluminum-GFRP plate at 250 kHz.

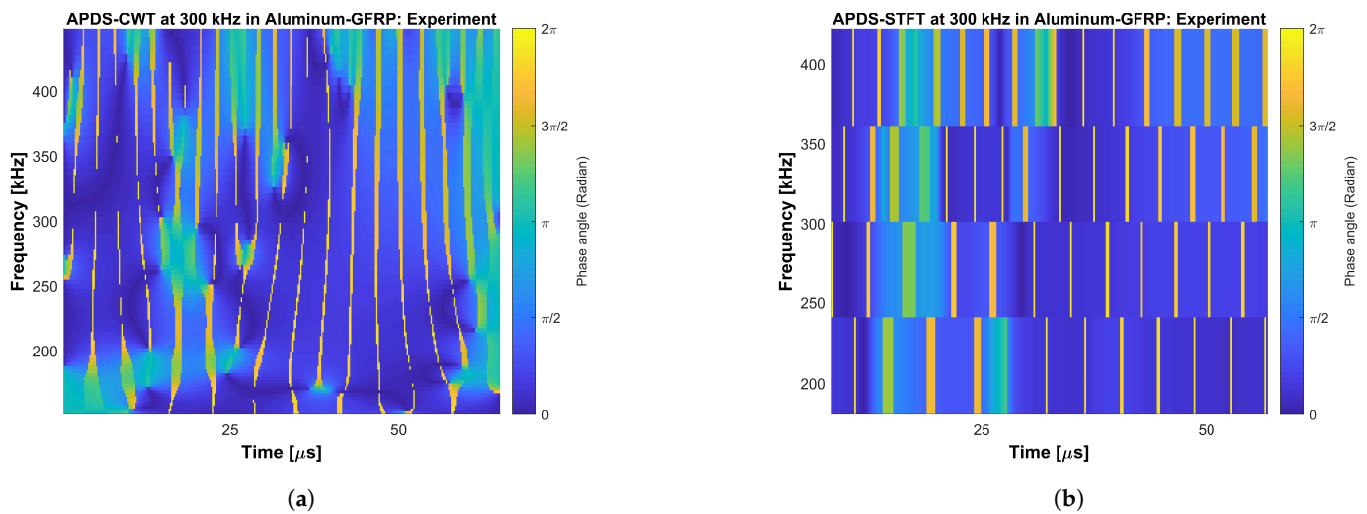


Figure A6. The APDS-CWT and APDS-STFT of the aluminum-GFRP plate at 300 kHz: the A_0 -mode is identified in the APDS-CWT and the APDS-STFT at the excitation center frequency. (a) APDS-CWT of the aluminum-GFRP plate at 300 kHz. (b) APDS-STFT of the Aluminum-GFRP plate at 300 kHz.

References

- Giurgiutiu, V. *Structural Health Monitoring with Piezoelectric Wafer Active Sensors*; Academic Press/Elsevier: Amsterdam, The Netherlands, 2008.
- Gabbert, U.; Sinapius, M.; Schuster, T.; Wierach, P.; Lammering, R. *Lamb-Wave Based Structural Health Monitoring in Polymer Composites*, 1st ed.; Research Topics in Aerospace; Springer International PU: Cham, Switzerland, 2017.
- Mustapha, S.; Ye, L. Leaky and non-leaky behaviours of guided waves in CF/EP sandwich structures. *Wave Motion* **2014**, *51*, 905–918. [[CrossRef](#)]
- Yuan, Y.O.; Bozdağ, E.; Ciardelli, C.; Gao, F.; Simons, F.J. The exponentiated phase measurement, and objective-function hybridization for adjoint waveform tomography. *Geophys. J. Int.* **2020**, *221*, 1145–1164. [[CrossRef](#)]
- Karrenberg, U. *Signale—Prozesse—Systeme: Eine Multimediale und Interaktive Einführung in die Signalverarbeitung*, 2nd ed.; Springer: Berlin/Heidelberg, Germany, 2005. [[CrossRef](#)]
- Su, Z.; Ye, L. (Eds.) *Identification of Damage Using Lamb Waves: From Fundamentals to Applications*; Lecture Notes in Applied and Computational Mechanics; Springer: Berlin/Heidelberg, Germany, 2009; Volume 48.
- Detection and quantification of pipe damage from change in time of flight and phase. *Ultrasonics* **2015**, *62*, 223–236. [[CrossRef](#)] [[PubMed](#)]
- van Quyen, M.; Foucher, J.; Lachaux, J.P.; Rodriguez, E.; Lutz, A.; Martinerie, J.; Varela, F.J. Comparison of Hilbert transform and wavelet methods for the analysis of neuronal synchrony. *J. Neurosci. Methods* **2001**, *111*, 83–98. [[CrossRef](#)] [[PubMed](#)]
- Roux, S.G.; Cenier, T.; Garcia, S.; Litaudon, P.; Buonviso, N. A wavelet-based method for local phase extraction from a multi-frequency oscillatory signal. *J. Neurosci. Methods* **2007**, *160*, 135–143. [[CrossRef](#)] [[PubMed](#)]
- Amjad, U.; Yadav, S.K.; Kundu, T. Detection and quantification of delamination in laminated plates from the phase of appropriate guided wave modes. *Opt. Eng.* **2015**, *55*, 011006. [[CrossRef](#)]
- Ambrozinski, L.; Magda, P.; Dragan, T.; Stepinski, T.; Uhl, T.; Chang, F.K. (Eds.) Temperature Compensation Based on Hilbert Transform and Instantaneous Phase for Lamb Waves-Based SHM Systems of Aircraft Structures // Structural health monitoring 2013: A roadmap to intelligent structures. In Proceedings of the 9th International Workshop on Structural Health Monitoring, Stanford, CA, USA, 10–12 September 2013.
- Barroso-Romero, M.; Gagar, D.; Pant, S.; Martinez, M. Wave Mode Identification of Acoustic Emission Signals Using Phase Analysis. *Acoustics* **2019**, *1*, 450–472. [[CrossRef](#)]
- Tiwari, K.A.; Raisutis, R. Identification and Characterization of Defects in Glass Fiber Reinforced Plastic by Refining the Guided Lamb Waves. *Materials* **2018**, *11*, 1173. [[CrossRef](#)] [[PubMed](#)]
- Chang, H.Y.; Yuan, F.G. Damage imaging in a stiffened curved composite sandwich panel with wavenumber index via Riesz transform. *Struct. Health Monit.* **2020**, *19*, 902–916. [[CrossRef](#)]
- Prado, V.T.; Granja, S.C.G.; Higuti, R.T.; Kitano, C.; Martínez-Graullera, Ó.; Segura, L.E. (Eds.) Defect Detection in Anisotropic Plates Based on the Instantaneous Phase of Signals. *IEEE Trans. Ultrason. Ferroelectr. Freq. Control.* **2015**, *62*, 1888–1894. [[CrossRef](#)] [[PubMed](#)]
- Tabatabaeipour, M.; Tzaferis, K.; McMillan, R.; Jackson, W.; Dobie, G.; Edwards, R.S.; Trushkevych, O.; Gachagan, A. Ultrasonic guided wave estimation of minimum remaining wall thickness using Gaussian process regression. *Mater. Des.* **2022**, *221*, 110990. [[CrossRef](#)]

17. Kim, J.; Park, Y.; Chung, W.; Kim, J.; Park, Y.; Chung, W. Transform based feature construction utilizing magnitude and phase for convolutional neural network in EEG signal classification. In Proceedings of the 2020 8th International Winter Conference on Brain-Computer Interface (BCI), Gangwon, Republic of Korea, 26–28 February 2020; pp. 1–4. [[CrossRef](#)]
18. Ni, S.H.; Yang, Y.Z.; Tsai, P.H.; Chou, W.H. Evaluation of pile defects using complex continuous wavelet transform analysis. *NDT E Int.* **2017**, *87*, 50–59. [[CrossRef](#)]
19. Hsueh, W.; Loh, C.. Damage detection of structures by wavelet analysis: Application to seismic response of steel frames 2017. In Proceedings of the SPIE. Sensors and Smart Structures Technologies for Civil, Mechanical, and Aerospace Systems 2017, Portland, OR, USA, 25–29 March 2017; pp. 201725–292017. [[CrossRef](#)]
20. Barth, T.; Wiedemann, J.; Roloff, T.; Hühne, C.; Sinapius, M.; Rauter, N. Investigations on Guided Ultrasonic Wave Dispersion Behavior in Fiber Metal Laminates Using Finite Element Eigenvalue Analysis. *Proc. Appl. Math. Mech.* **2022**. *accepted for publication*. [[CrossRef](#)]
21. Gunnik, J.W.; Vlot, A. *Fibre Metal Laminates: An Introduction*; Springer: Dordrecht, The Netherlands, 2001.
22. Döring, D. *Eine Kurze Einführung in die Systemtheorie: Lehr- und Übungsbuch*; Vieweg+Teubner Verlag/Springer Fachmedien Wiesbaden GmbH Wiesbaden: Wiesbaden, Germany, 2011. [[CrossRef](#)]
23. Küpfmüller, K.; Kohn, G. *Theoretische Elektrotechnik und Elektronik: Eine Einführung*, 14th ed.; Springer: Berlin/Heidelberg, Germany, 1993.
24. Lilly, J.M.; Olhede, S.C. Higher-Order Properties of Analytic Wavelets. *IEEE Trans. Signal Process.* **2009**, *57*, 146–160. [[CrossRef](#)]
25. MathWorks Help Center Documentation: Time-Frequency Gallery. Available online: <https://de.mathworks.com/help/signal/ug/time-frequency-gallery.html> (accessed on 17 December 2021).
26. Zhivomirov, H. STFT and ISTFT with Matlab Implementation. *TEM J.* **2019**, *8*, 56–64. [[CrossRef](#)]
27. MathWorks Help Center Documentation: Continuous 1-D Wavelet Transform. Available online: <https://www.mathworks.com/help/wavelet/ref/cwt.html> (accessed on 7 December 2022).
28. MathWorks Help Center Documentation: Continuous Wavelet Transform Filter Bank. Available online: <https://de.mathworks.com/help/wavelet/ref/cwtfilterbank.html> (accessed on 7 October 2022).
29. Moser, F.; Jacobs, L.J.; Qu, J. Modeling elastic wave propagation in waveguides with the finite element method. *NDT E Int.* **1999**, *32*, 225–234. [[CrossRef](#)]
30. Rauter, N.; Lammering, R. A constitutive model for the analysis of second harmonic Lamb waves in unidirectional composites. *Int. J. Solids Struct.* **2018**, *135*, 184–196. [[CrossRef](#)]

Disclaimer/Publisher’s Note: The statements, opinions and data contained in all publications are solely those of the individual author(s) and contributor(s) and not of MDPI and/or the editor(s). MDPI and/or the editor(s) disclaim responsibility for any injury to people or property resulting from any ideas, methods, instructions or products referred to in the content.